A multi-scale framework to predict damage initiation at martensite/ferrite interface

Liu, L.; Maresca, F.; Hoefnagels, J. P.M.; Geers, M. G.D.; Kouznetsova, V. G.

Published in:
Journal of the Mechanics and Physics of Solids

DOI:
10.1016/j.jmps.2022.105018

Publication date:
2022

J. Mech. Phys. Solids 168 (2022) 105018

Contents lists available at ScienceDirect

Journal of the Mechanics and Physics of Solids

journal homepage: www.elsevier.com/locate/jmps

A multi-scale framework to predict damage initiation at martensite/ferrite interface

L. Liu [a,b], F. Maresca [c], J.P.M. Hoefnagels [a], M.G.D. Geers [a], V.G. Kouznetsova [a,*]

[a] Department of Mechanical Engineering, Eindhoven University of Technology, 5600 MB Eindhoven, The Netherlands
[b] Materials Innovation Institute (M2i), 2600 GA Delft, The Netherlands
[c] Engineering and Technology Institute Groningen, Faculty of Science and Engineering, University of Groningen, 9747 AG Groningen, The Netherlands

ARTICLE INFO

Keywords:
Multi-scale framework
Dual-phase steel
Martensite/ferrite interface
Damage initiation
Substructure boundary sliding
Interface orientation

ABSTRACT

Martensite/ferrite (M/F) interface damage largely controls failure of dual-phase (DP) steels. In order to predict the failure and assess the ductility of DP steels, accurate models for the M/F interfacial zones are needed. Several M/F interface models have been proposed in the literature, which however do not incorporate the underlying microphysics. It has been recently suggested that (lath) martensite substructure boundary sliding dominates the M/F interface damage initiation and therefore should be taken into account. Considering the computationally infeasibility of direct numerical simulations of statistically representative DP steel microstructures, while explicitly resolving the interface microstructures and the sliding activity, a novel multi-scale approach is developed in this work. Two scales are considered: the DP steel mesostructure consisting of multiple lath martensite islands embedded in a ferrite matrix, and the microscopic M/F interfacial zone unit cell resolving the martensite substructure. Based on the emerging microscopic damage initiation pattern, an effective indicator for the M/F interface damage initiation is determined from the interface microstructural unit cell response, along with the effective sliding in this unit cell. Relating these two effective quantities for different interface microstructural configurations leads to an effective mesoscale model relating the interface damage indicator to the sliding activity of the martensite island in terms of the mesoscopic kinematics. This microphysics-based M/F interface damage indicator model, which could not be envisioned a-priori, is fully identified from a set of interfacial unit cell simulations, thus enabling the efficient prediction of interface damage initiation at the mesoscale. The capability of the developed effective model to predict the mesoscopic M/F interface damage initiation is demonstrated on an example of a realistic DP steel mesostructure.

1. Introduction

Because of the excellent mechanical performance and high cost efficiency, dual-phase (DP) steels consisting of a ferrite/(lath) martensite microstructure are nowadays among the most widely used advanced high strength steels (AHSS) developed for the automotive industry (Lutsey, 2010). One of the most important objectives in the design of DP steels is to improve strength and ductility simultaneously. Several attempts to increase the strength of DP steels by tailoring different microstructural features have been carried out (Sun and Pugh, 2002; Mazinani and Poole, 2007; Pierman et al., 2014; Calcagnotto et al., 2010), which however

* Corresponding author.
E-mail address: v.g.kouznetsova@tue.nl (V.G. Kouznetsova).

https://doi.org/10.1016/j.jmps.2022.105018
Received 15 April 2022; Received in revised form 15 July 2022; Accepted 29 July 2022
Available online 8 August 2022

were often accompanied by a ductility decrease. This strength/ductility trade-off is a critical challenge for future of DP steels, as required for the manufacturing of light-weight complex structural components.

In order to overcome this trade-off, the physics and mechanics of DP steel failure must be understood. Based on extensive experimental data, it has been concluded that martensite/ferrite (M/F) interface damage dominates failure of most widely used DP grades (Tasan et al., 2014). Moreover, the voids nucleated at the M/F interface are able to grow easily, due to the limited mechanical constraints from the surrounding ferrite matrix (Maire et al., 2008; Isik et al., 2016). These facts motivate the detailed investigation and modelling of M/F interfaces to predict failure and assess the ductility of DP steels (Tang et al., 2021).

Hence, several approaches have been proposed in the literature for M/F interface modelling at the mesoscale, i.e. the scale representing multiple lath martensite islands embedded in a ferrite matrix. For example, Kadkhodapour et al. (2011), Sodjit and Uthaisangsuk (2012) and Abid et al. (2017) modelled the M/F interfaces as separate interphase layers with a predefined finite thickness and material properties, enabling to account for local hardening effects induced by interfacial dislocations. Uthaisangsuk et al. (2011), Hosseini-Toudeshky et al. (2015) and Kim et al. (2017) modelled the M/F interfaces as cohesive zones within a finite element method (FEM) framework and investigated damage initiation and propagation along the interfaces, leading to failure of DP steels. However, the sharp cohesive zone approach contradicts detailed experimental observations which show that damage often does not occur exactly at the interface, but propagates towards the near-interface ferrite (see e.g. Hoefnagels et al., 2015). Later, Ahmadi et al. (2020) reformulated the M/F interphase layer model within a peridynamic framework, demonstrating more flexibility compared to FEM-based cohesive zone M/F interface modelling. Nevertheless, these M/F interface/interphase models typically lack a clear definition of the interface/interphase zone, often rely on ad-hoc assumptions for the model parameters and do not always incorporate relevant microscale phenomena.

Recently, it has been shown that the M/F interface damage can be triggered by lath martensite substructure boundary sliding (Liu et al., 2021), acting as an intrinsic feature of martesnite, which was widely confirmed by detailed experimental observations on several fully martensitic steels (Du et al., 2016; Inoue et al., 2019; Ghaffarian et al., 2022) and different DP steels (Du et al., 2019; Tian et al., 2020). This sliding-triggered interface damage phenomenon was originally hypothesized in a systematic crystal plasticity study (Liu et al., 2021), which accounted for different loading conditions, phase contrasts, residual stresses/strains, as well as a range of possible M/F interfacial morphologies. Later, the sliding-triggered M/F interface damage initiation has also been suggested by experimental observations[1] (Vermeij et al., 2022a), as shown in Figs. 1(a–b). One possible physical explanation of this sliding mechanism is the presence of inter-lath retained austenite (RA) films on which the hard martensite laths (ML) can easily slide (Maresca et al., 2014a,b), either via dislocation-mediated plasticity or through martensitic phase transformation upon mechanical loading, which can lead to similar apparent sliding behaviour (Maresca et al., 2018). The substructure boundary sliding mechanism is facilitated by the specific martensite/austenite (M/A) crystallographic orientation relationship (OR) and the lower slip resistance of the FCC austenite films compared to the BCC laths. The presence of these RA films have been experimentally confirmed at lath boundaries in a broad range of fully martensitic steels (Sandvik and Wayman, 1983; Kelly et al., 1990; Morito et al., 2011) and some DP steels (Liao et al., 2010; Yoshida et al., 2015). However, since these layers can be very thin, they are difficult to identify experimentally, in particular in DP steels. In the literature (see e.g. Ohmura et al., 2004; Morsdorf et al., 2016; Ghaffarian et al., 2022), an alternative explanation of the substructure boundary sliding without introducing the RA films has also been proposed, as the dislocation glide on the lath interfacial planes, which however has less experimental confirmation. Therefore, without loss of generality, in this contribution, the assumption on the RA films will be adopted to model martensite substructure boundary sliding.

Since the martensite islands in DP steels have generally only few variants, such that the internal boundaries cross almost the whole islands (Chehab et al., 2010), the substructure boundary sliding acts as favourable deformation mode, as shown numerically in Maresca et al. (2016a) and experimentally in Du et al. (2019). This can induce large plastic strain concentration in the near-interface ferrite around the RA film tips and promote M/F interface damage initiation (Liu et al., 2021), as shown in Figs. 1(c–d), where the plastic strain has been exploited as an indicator for the damage initiation. Similar strain localization phenomena have been observed in recent microscopic digital image correlation measurements (Vermeij et al., 2022b), revealing a set of discrete strain localization traces following the martensite substructure boundaries and continuing towards the ferrite. Therefore, it is important that the mentioned substructure boundary sliding mechanism is taken into account in the M/F interface modelling.

However, the evaluation of the onset of M/F interface damage by performing direct numerical simulations of statistically representative DP steel microstructures consisting of M/F interfaces involving different geometrical and crystallographic orientations, multiple substructural features, e.g. thin inter-lath RA films (Maresca et al., 2014a,b), complex interfacial morphologies (Liu et al., 2021), precipitates, etc., is computationally prohibitive. This calls upon a multi-scale approach incorporating consistent interface descriptions at different scales, which provides an efficient and accurate microphysics-based prediction of the M/F interface damage initiation in DP steel mesostructures. To the best knowledge of the authors, such a multi-scale framework is currently not available in the literature and will therefore be developed in the present work.

This paper is organized as follows. The outline of the multi-scale framework to be established for the prediction of M/F interface damage initiation is given in Section 2. The microscopic M/F interfacial zone unit cell problem description and simulation setup are detailed in Section 3. The main governing mesoscale quantities, i.e. the effective martensite island sliding and the effective M/F interface damage indicator, are defined in Section 4. In Section 5, these effective quantities are extracted from a set of representative

[1] Detailed experimental methods and results are reported in Vermeij et al. (2022a), including the justification and analysis of the martensite substructure boundary sliding in DP steels and the sliding-triggered M/F interface damage initiation.

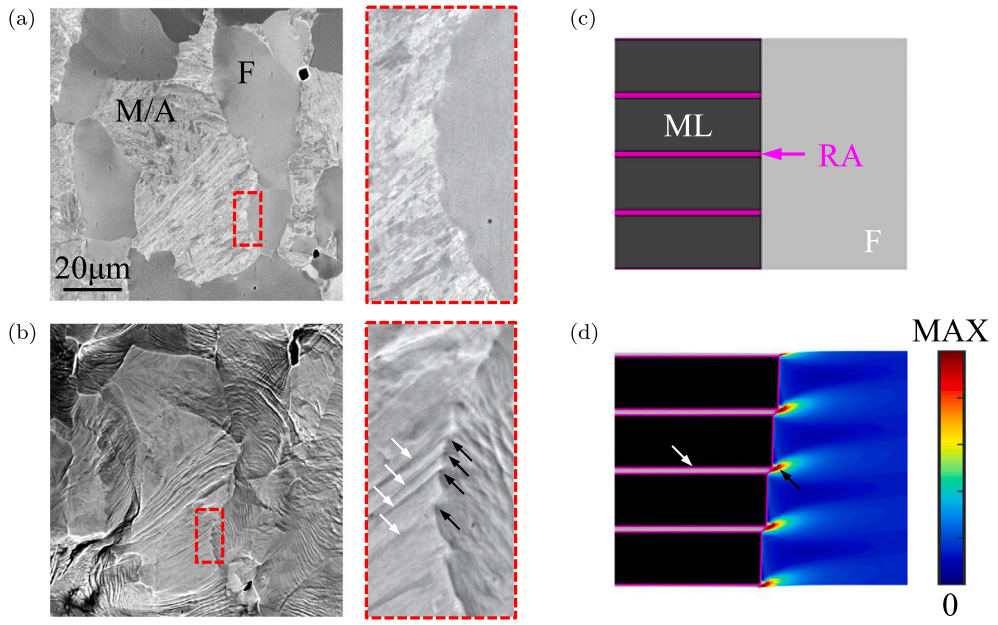

Fig. 1. SEM micrographs of a DP steel specimen in the (a) undeformed and (b) deformed states, showing active substructure boundary sliding within the central martensite island (martensite/austenite laminate, M/A). The magnifications of the M/F interface (red box) reveal the interfacial morphology and interface damage initiation (black arrows) triggered by substructure boundary sliding (white arrows). (a–b) reproduced from Vermeij et al. (2022a) with permission from the authors; (c) fully resolved M/F interface model with retained austenite (RA) films between the martensite laths (ML) and (d) the corresponding plastic strain map (with the value range represented by a colorbar) in the near-interface ferrite in case of active substructure boundary sliding, showing damage initiation around the RA film tips. (c–d) reproduced from Liu et al. (2021) with permission from Elsevier.

unit cell simulations and then related to each other through an effective mesoscale constitutive model established and quantitatively identified in Section 6. The applicability of this microphysics-based M/F interface damage indicator model to the analysis of the M/F interface damage 'hot spots' in a realistic DP mesostructure containing multiple lath martensite islands is demonstrated in Section 7. Finally, the conclusions are given in Section 8.

Scalars, vectors, second-order tensors and fourth-order tensors adopted throughout this paper are denoted as a, $\vec{a}$, $\mathbf{A}$ and $\mathbb{A}$, respectively. The following notation for vector and tensor product operations is employed together with Einstein's summation convention: the dyadic product $\vec{a} \otimes \vec{b} = a_i a_j \vec{e}_i \vec{e}_j$ and the dot product $\mathbf{A} \cdot \mathbf{B} = A_{ij} B_{jk} \vec{e}_i \vec{e}_k$, with $\{\vec{e}_x, \vec{e}_y, \vec{e}_z\}$ the Cartesian vector basis. The length of a vector (Euclidean norm) is denoted by $\|\vec{\bullet}\|$. The inverse of a second-order tensor is indicated by $(\bullet)^{-1}$.

2. Multi-scale framework

The multi-scale framework established in this work considers two spatial scales and consists of an 'off-line' pre-computation stage and an 'on-line' simulation stage, as sketched in Fig. 2. The coarse scale represents the scale of the multi-phase structure of the DP steel, consisting of lath martensite islands in a ferrite matrix. This scale will be here called *mesoscale*. In the literature (see e.g. de Geus et al., 2016; Tang et al., 2021), the damage onset is often evaluated using an indicator which serves to quantify the chance of the damage initiation and is computed by post-processing the obtained mechanical response. Moreover, as explained in the Section 1, the focus of this work is on the dominating sliding-triggered damage initiation mode in the ferrite matrix near the M/F interface. The goal is therefore to obtain a model that will provide an indicator for the damage initiation in this interfacial zone $\mathcal{D}_{\mathrm{IZ}}$ as a function of the deformation gradient tensor $\mathbf{F}_{\mathrm{M/A}}$ of the near-interface martensite. The model relies on the numerical investigations previously established in Liu et al. (2021) and supported by the experiments in Du et al. (2019), Vermeij et al. (2022a,b), as discussed in the Section 1. The resulting hypothesis is:

> *The martensite substructure boundary sliding dominates the M/F interface damage initiation by inducing large plastic strain concentration in the near-interface ferrite around the RA film tips.*

To capture this fine scale mechanism, *microscale* interfacial zone unit cell models are considered consisting of a ferrite matrix adjacent to a martensite lath with the RA film inserted to model the substructure boundary sliding, see Fig. 2. The behaviour of these unit cells is first analysed in an 'off-line' stage of the model, which includes the following steps:

- A set of representative loading conditions $\mathcal{F}_{\mathrm{IZ}}$, which sample the space of the sliding directions, are predefined and applied on the microscopic M/F interfacial zone unit cells for different interface orientations. Details of the unit cell problem description and the simulation setup will be introduced in Section 3.

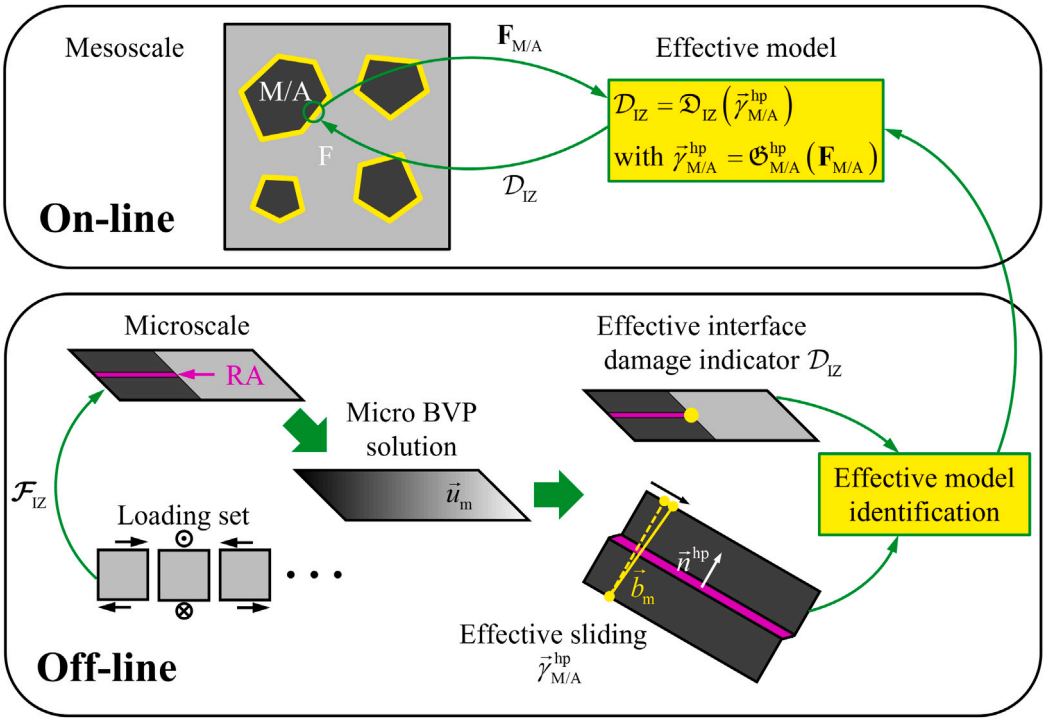

Fig. 2. Schematic overview of the multi-scale framework to predict M/F interface damage initiation, where an effective interface damage indicator model is constructed based on off-line unit cell simulations, which are exploited in the on-line mesoscopic simulations.

- After solving the microscopic quasi-static boundary value problem (BVP) for each loading case, the results are post-processed to extract the effective M/F interface damage indicator $\mathcal{D}_{IZ}$ and the effective sliding $\vec{\gamma}^{hp}_{M/A}$ of the martensite island. Definitions of these effective quantities will be given in Section 4.
- Next, $\mathcal{D}_{IZ}$ and $\vec{\gamma}^{hp}_{M/A}$ for each unit cell with a specific interface orientation are correlated with each other. On the basis of this correlation, an effective mesoscale interface damage indicator function $\mathcal{D}_{IZ} = \mathfrak{D}_{IZ}(\vec{\gamma}^{hp}_{M/A})$ is extracted. Section 6 will present the formulation and parameter identification of this effective model, based on the results of the microscale unit cell simulations given in Section 5.

It should be emphasized, that the off-line stage only needs to be performed once.

The 'on-line' stage concerns the solution of the quasi-static BVP for a representative mesoscopic model, see Fig. 2. Here, for each (integration) point in the near-interface martensite, the deformation gradient tensor $\mathbf{F}_{M/A}$ is first used to evaluate the effective sliding $\vec{\gamma}^{hp}_{M/A}$, depending on the interface orientation and the martensite habit plane orientation. With this, the effective interface damage indicator model is used to compute the damage indicator $\mathcal{D}_{IZ} = \mathfrak{D}_{IZ}(\vec{\gamma}^{hp}_{M/A})$, indicating the locations of interface damage 'hot spots', i.e. where the damage tends to occur first (see e.g. de Geus et al., 2016; Tang et al., 2021). The application of this model on a realistic DP mesostructure will be demonstrated in Section 7.

3. Microscopic unit cell

Consider a typical DP steel mesostructure $\mathcal{V}$ with external boundary $\mathcal{S}$, sketched in Fig. 3(a), which reveals a few lath martensite islands $\mathcal{V}_{M/A}$ embedded in a ferrite matrix $\mathcal{V}_F$, with the M/F interfaces indicated by $\mathcal{S}_{M/F}$. The mesoscopic M/F interfacial zone $\mathcal{V}_{IZ}$ with external boundary $\mathcal{S}_{IZ}$, is defined as a small material volume surrounding a part of $\mathcal{S}_{M/F}$, with the local normal indicated by $\vec{N}_{M/F}$, as shown in Fig. 3(b). The underlying M/F interface microstructure is sketched in Fig. 3(c), revealing the detailed underlying martensite substructure: the martensite consists of a stack of laths and RA films. Only an initially straight interface between the laths and the ferrite matrix is considered here, based on the conclusions in Liu et al. (2021) stating that when sliding is active, the specific interfacial morphology plays a secondary role on the M/F interface damage initiation. The normal to the RA film at the RA/F interface is denoted by $\vec{N}_{RA/F}$, which in the considered setup coincides with $\vec{N}_{M/F}$ in the initial, undeformed configuration. Each lath is flat and elongated along the habit plane, the normal of which is denoted by $\vec{N}^{hp}$. Since the lath thickness is much smaller compared to its in-habit-plane dimensions and the overall size of the martensite (Krauss and Marder, 1971; Morito et al., 2003, 2006), it is fair to assume periodicity in the direction of the habit plane normal and in the lath long direction. Thus, a unit cell $\mathcal{V}_m$ (with subscript "m" denoting the microscale) is defined (see Fig. 3(d)) representing the M/F interface microstructure.

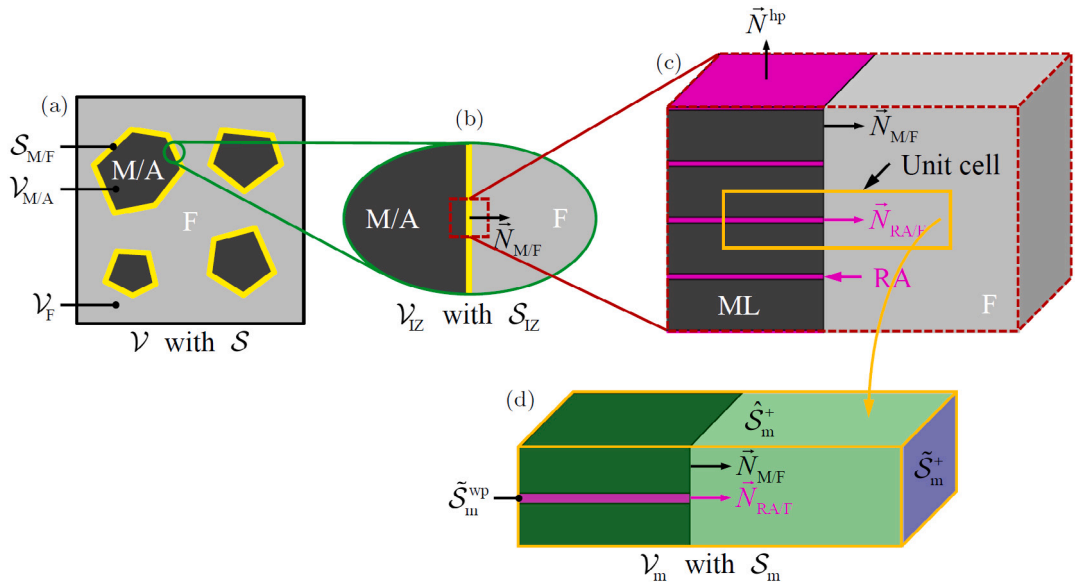

Fig. 3. (a) A DP steel mesostructure consisting of a few lath martensite islands embedded in a ferrite matrix. The M/F interfaces are indicated by the yellow lines; (b) magnification of a mesoscopic M/F interfacial zone containing a part of the M/F interface; (c) underlying M/F interface microstructure resolving the martensite substructure with RA films, from which a microscopic M/F interfacial zone unit cell is defined, indicated by the orange box; (d) the microscopic M/F interfacial zone unit cell with the boundary parts $\tilde{\mathcal{S}}_{\mathrm{m}}$ and $\bar{\mathcal{S}}_{\mathrm{m}}$, indicated by the green and blue shadows, respectively. The boundaries $\tilde{\mathcal{S}}_{\mathrm{m}}^{-}$ and $\bar{\mathcal{S}}_{\mathrm{m}}^{-}$ opposite to $\tilde{\mathcal{S}}_{\mathrm{m}}^{+}$ and $\bar{\mathcal{S}}_{\mathrm{m}}^{+}$, respectively, are not visible in (d).

To represent the periodicity of the unit cell in the direction of the habit plane normal, and in the lath long direction, periodic boundary conditions are applied on the unit cell surfaces $\tilde{\mathcal{S}}_{\mathrm{m}}^{-/+}$ perpendicular to the interface, shaded green in Fig. 3(d). On the surfaces $\bar{\mathcal{S}}_{\mathrm{m}}^{-/+}$ parallel to the interface, shaded blue in Fig. 3(d), periodicity constraints may not be applied. For these surfaces, customized boundary conditions are used, which allow independent microfluctuations on the surfaces crossing the martensite and ferrite phases. Moreover, special care is taken to prevent spurious excessive deformation of the weak phase (denoted by superscript "wp"), RA film boundary part $\tilde{\mathcal{S}}_{\mathrm{m}}^{\mathrm{wp}}$. These boundary conditions are detailed in Appendix A.

Since the interface orientation with respect to the habit plane may vary at different locations within one martensite island and between the islands, a more general configuration of the microscopic M/F interfacial zone unit cell simulated here is further introduced in Fig. 4(a). Angle $\theta^{\mathrm{hp}} = \arccos(\vec{N}_{\mathrm{RA/F}} \cdot \vec{N}^{\mathrm{hp}})$ denotes the initial, undeformed configuration, angle between the RA/F interface (or the M/F interface) and the habit plane. Simulations on the unit cells with different θ^{hp} will be performed. For convenience of numerical implementation and post-processing, the configuration of each unit cell with $\theta^{\mathrm{hp}} \neq 90°$ has been rotated such that the M/F interface normal $\vec{N}_{\mathrm{M/F}}$ coincides with the positive X axis, see the example for $\theta^{\mathrm{hp}} = 45°$ in Fig. 4(b).

The reference unit cell dimensions are as follows, see Fig. 4(a). The unit cell thickness is taken as $T = 100$ nm (Yoshida et al., 2015), while the RA film thickness is taken as $r = 10$ nm (estimated from the TEM images in Liao et al., 2010), leading to a lath thickness $T_{\mathrm{ML}} = T - r = 90$ nm. Assuming an interfacial zone martensite (together with the RA films) volume fraction $\eta_{\mathrm{M/A}} = 44.4\%$, the unit cell length is $L = 375$ nm, resulting in a RA volume fraction $\eta_{\mathrm{RA}} = 4.44\%$, the length of the martensite domain $l = 167$ nm and the length of the ferrite domain $L_{\mathrm{F}} = L - l = 208$ nm, respectively. Note, that $\eta_{\mathrm{M/A}}$ represents the martensite volume fraction within the interfacial zone, which is *independent* of the martensite volume fraction in the DP steel mesostructure (as to be used in Section 7).

Each unit cell is discretized using three-dimensional (3D) quadratic finite elements with one element in the out-of-plane Z direction. To enable comparisons, the near-interface finite element mesh sizes for different unit cells are set to ~2.5 nm. The resulting in-plane finite element discretizations of the two unit cells with $\theta^{\mathrm{hp}} = 90°$ and $\theta^{\mathrm{hp}} = 45°$, respectively, are shown in Fig. 4(b) as examples. A mesh sensitivity check has been performed and confirmed that both local and global responses are converged for the adopted discretization for each unit cell. Besides, it has been verified that by using the proposed boundary conditions, the reshaped and original configurations lead to consistent local and global responses, and the results are insensitive to the choice of the unit cell length L and martensite volume fraction $\eta_{\mathrm{M/A}}$ as long as L is sufficiently large, which is the case for $L = 375$ nm.

BCC laths and FCC RA films are modelled as single crystals with the Kurdjumov–Sachs (KS) orientation relationship (OR). The BCC lath KS variant $(111)_{\gamma} \parallel (011)_{\alpha'}$, $[10\bar{1}]_{\gamma} \parallel [11\bar{1}]_{\alpha'}$ is selected for the simulations. Corresponding crystallographic axes are illustrated in Fig. 4(a), together with the global coordinate system. It has been verified that for the cases where substructure boundary sliding is highly active, which are of interest here, the plastic deformation of the unit cell is insensitive to the above BCC lath variant choice, because of the low RA fiflm anisotropy in the habit plane and the negligible lath plasticity.

A finite deformation crystal plasticity model with cubic elasticity (see e.g. Kalidindi et al., 1992) is employed to describe the material behaviour of both BCC laths and FCC RA films, including the OR. The crystal plasticity model is implemented using the

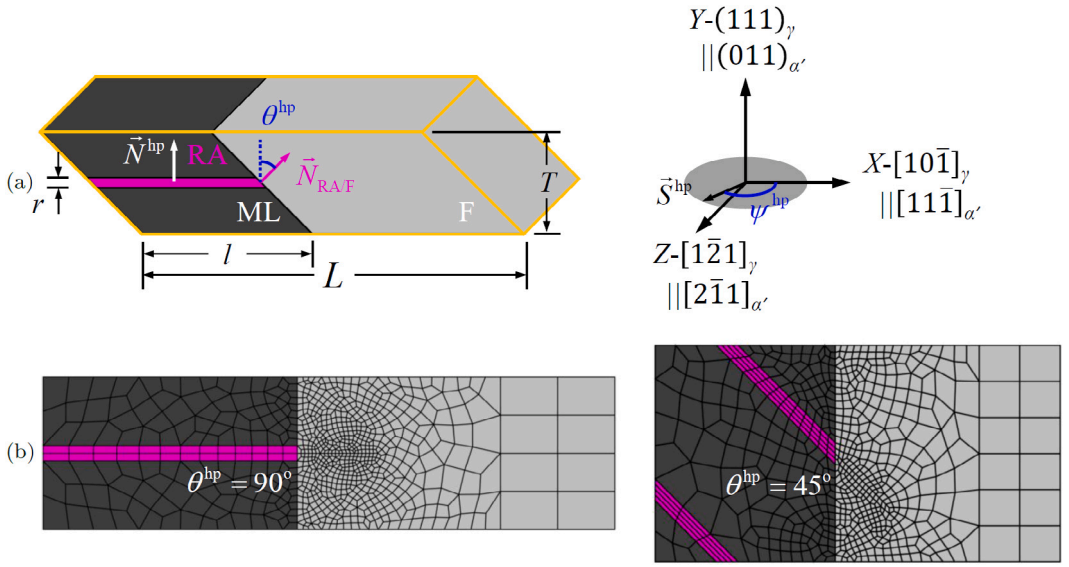

Fig. 4. (a) Geometrical model configuration of a microscopic M/F interfacial zone unit cell with the M/F interface orientation defined by the angle θ^{hp}. The orientations of the BCC lath (α') and FCC RA film (γ) crystallographic axes, and the global coordinate system are also shown; (b) in-plane finite element meshes of two selected unit cells.

Table 1
Material parameters of the martensite island.

Parameter	Symbol	Martensite lath	RA film
Elasticity component 11	C_{11}	349 [GPa]	268 [GPa]
Elasticity component 12	C_{12}	202 [GPa]	156 [GPa]
Elasticity component 44	C_{44}	176 [GPa]	136 [GPa]
Reference slip rate	$\dot{\gamma}_0$	0.01 [s^{-1}]	0.01 [s^{-1}]
Initial slip resistance	s_0	0.765 [GPa]	0.265 [GPa]
Saturation slip resistance	s_∞	3 [GPa]	0.34 [GPa]
Reference hardening modulus	h_0	2.25 [GPa]	0.25 [GPa]
Slip rate sensitivity	m	0.05 [–]	0.05 [–]
Hardening exponent	n	1.5	1.5
Latent/self hardening ratio	q	1.4	1.4
Slip family	$\{\vec{n}\}\langle\vec{s}\rangle$	$\{110\}_{\alpha'}\langle 111\rangle_{\alpha'}$ $\{112\}_{\alpha'}\langle 111\rangle_{\alpha'}$	$\{111\}_\gamma\langle 110\rangle_\gamma$

Table 2
Material parameters of the ferrite matrix.

Parameter	Symbol	F matrix
Young's modulus	E	200 [GPa]
Poisson's ratio	ν	0.3 [–]
Initial yield stress	S_0	0.45 [GPa]
Saturation yield stress	S_∞	0.678 [GPa]
Characteristic strain	E_c	0.0351 [–]

user-defined subroutine HYPELA2.F, supported in the commercial FEM package MSC.MARC. There is no clear evidence of a preferential crystallographic orientation of the BCC ferrite grains with respect to the martensite islands in DP steels. Supported by the findings in de Geus et al. (2016), ferrite grain orientation effects are neglected here for simplicity, and a finite strain isotropic elasto-plasticity model is used to describe the behaviour of the ferrite matrix. This assumption is also supported by recent detailed experimental investigations (Tian et al., 2020), showing that for ferrite in DP steels, any of the 48 slip systems of the {110}, {112} and {123} families may activate at comparable stress levels and according to Schmid's law, making the ferrite plastic behaviour nearly isotropic (see Raabe et al., 2001 for the anisotropic yield surface evolution as the number of slip systems increases). This is further supported by the fact that isotropic elasto-plastic ferrite has been shown to be a sufficiently accurate approximation as long as the M/F phase contrast is > 4 (de Geus et al., 2016), which is the case in the present study. More details about the material models of the martensite island and the ferrite matrix can be found in Appendix B. The material parameters used in the simulations are taken from Liu et al. (2021), and listed in Tables 1 and 2.

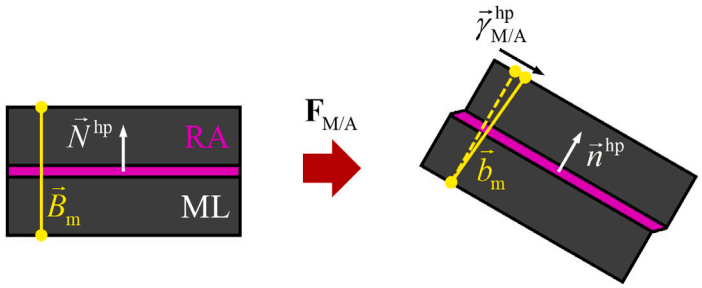

Fig. 5. 2D sketch of the effective sliding $\vec{\gamma}^{\mathrm{hp}}_{\mathrm{M/A}}$ between the initial undeformed configuration (left) and the current deformed configuration (right).

4. Definition of the effective quantities

4.1. Effective sliding

To quantify the sliding activity within the M/F interfacial zone unit cell, an effective sliding $\vec{\gamma}^{\mathrm{hp}}_{\mathrm{M/A}}$ of the martensite island is next defined based on the martensite substructure kinematics. Consider a simplified representation of a martensite island consisting of martensite laths with the same habit plane orientation and the RA films between the laths. The deformation of this martensite island is described by the overall deformation gradient tensor $\mathbf{F}_{\mathrm{M/A}}$, see Fig. 5. Let us denote a fibre through the thickness of the martensite island (i.e. in the direction of the habit plane normal $\vec{N}^{\mathrm{hp}}$) by $\vec{B}_{\mathrm{m}}$ in the initial configuration, which becomes $\vec{b}_{\mathrm{m}}$ after deformation, while the habit plane normal becomes $\vec{n}^{\mathrm{hp}}$. In case of inactive sliding, this fibre simply follows the rotation of the habit plane normal, while in the case of active sliding (and neglecting the small plastic deformation of the laths), additional effective shear takes place along the habit plane. Hence, an effective sliding vector of the martensite island can be defined by tracking the deformation of this fibre and the rotation of the habit plane normal (Liu et al., 2021):

$$\vec{\gamma}^{\mathrm{hp}}_{\mathrm{M/A}} \equiv (\mathbf{I} - \vec{n}^{\mathrm{hp}} \otimes \vec{n}^{\mathrm{hp}}) \cdot \frac{\vec{b}_{\mathrm{m}}}{\|\vec{B}_{\mathrm{m}}\|}, \tag{1}$$

with $\mathbf{I}$ the second-order identity tensor. The 2D interpretation of $\vec{\gamma}^{\mathrm{hp}}_{\mathrm{M/A}}$ is depicted in Fig. 5, showing that $\vec{\gamma}^{\mathrm{hp}}_{\mathrm{M/A}}$ is indeed the effective shear deformation component of the martensite island along the habit plane.

Although Eq. (1) provides an intuitive definition of $\vec{\gamma}^{\mathrm{hp}}_{\mathrm{M/A}}$, for the development of the multi-scale model, it is convenient to express Eq. (1) in terms of the overall deformation gradient tensor of the martensite island, $\mathbf{F}_{\mathrm{M/A}}$. Making use of $\vec{b}_{\mathrm{m}} = \mathbf{F}_{\mathrm{M/A}} \cdot \vec{B}_{\mathrm{m}}$, Eq. (1) can be rewritten as

$$\vec{\gamma}^{\mathrm{hp}}_{\mathrm{M/A}} = (\mathbf{I} - \vec{n}^{\mathrm{hp}} \otimes \vec{n}^{\mathrm{hp}}) \cdot (\mathbf{F}_{\mathrm{M/A}} \cdot \vec{N}^{\mathrm{hp}}). \tag{2}$$

Assuming that the volume of the martensite island and the surface area of the habit plane do not change, the current habit plane normal $\vec{n}^{\mathrm{hp}}$ used in Eq. (2) can be computed using Nanson's formula as

$$\vec{n}^{\mathrm{hp}} = \vec{N}^{\mathrm{hp}} \cdot \mathbf{F}^{-1}_{\mathrm{M/A}}. \tag{3}$$

Eq. (2) enables the evaluation of the effective sliding activity $\vec{\gamma}^{\mathrm{hp}}_{\mathrm{M/A}}$ directly at the mesoscale.

4.2. Effective interface damage indicator

It is assumed that the microscopic damage indicator model for the ferrite matrix can be written in a general form in terms of the microscopic plastic deformation gradient $\mathbf{F}_{\mathrm{m,p}}$ and the microscopic stress (state) $\mathbf{P}_{\mathrm{m}}$ as $\mathcal{D}_{\mathrm{m}}(t) = \mathfrak{D}_{\mathrm{m}}\left(\mathbf{F}_{\mathrm{m,p}}(t), \mathbf{P}_{\mathrm{m}}(t)\right)$, with t indicating the time. Since precipitates and ferrite grain boundaries are rarely involved at the scale of the M/F interfacial zone unit cell, only the intra-grain void nucleation is assumed here as a relevant mechanism for damage initiation in ferrite. Potential nano-micro-void nucleation in the near-interface ferrite (Ghadbeigi et al., 2013) physically originates from dislocation interactions, e.g. relaxation of the dislocation pile-ups and annihilation of the dislocations gliding on intersecting paths of different slip planes (Furukimi et al., 2017). Based on this mechanism and following the near-interface ferrite damage indicator choice[2] in Liu et al. (2021) (see also Fig. 1), the equivalent plastic strain rate $\dot{\varepsilon}^{\mathrm{eq}}_{\mathrm{m,p}}$ in the ferrite matrix $\mathcal{V}_{\mathrm{m,F}}$ will be used here as the microscopic damage indicator rate for the damage initiation in the M/F interfacial zone, i.e.

$$\dot{\mathcal{D}}_{\mathrm{m}} = \dot{\varepsilon}^{\mathrm{eq}}_{\mathrm{m,p}} \quad \text{in } \mathcal{V}_{\mathrm{m,F}}. \tag{4}$$

[2] A sensitivity study of the M/F interface damage initiation analysis with respect to the specific choice of the damage indicator is conducted in Liu et al. (2021), showing that within the active sliding regime, all considered damage indicators (including those accounting for stress triaxiality effects) lead to qualitatively similar results.

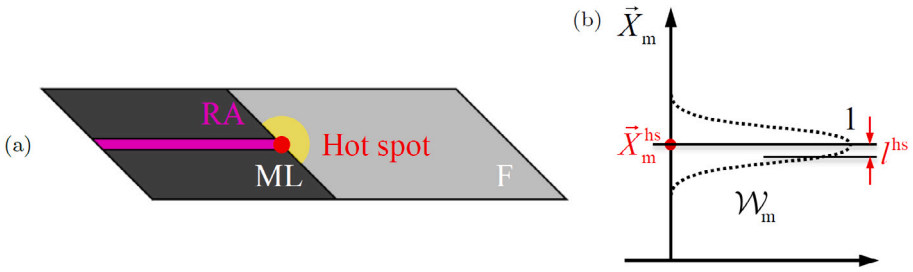

Fig. 6. (a) Schematic of the sliding-triggered interface damage 'hot spot' in the near-interface ferrite in the microscopic M/F interfacial zone unit cell. The hot spot location and the affected volume (exaggerated for clarity) are indicated by the red dot and yellow shadow, respectively; (b) 1D sketch of the weight function $\mathcal{W}_{\mathrm{m}}$, centred at the hot spot position $\vec{X}^{\mathrm{hs}}_{\mathrm{m}}$, with a length scale l^{hs}.

Note, that other choices for $\mathcal{D}_{\mathrm{m}}$ (see e.g. Rice and Tracey, 1969; Johnson and Cook, 1985; Wan et al., 2014, where the influence of stress state is also incorporated) are possible and can be directly used in the developed framework.

To upscale the microscopic damage indicator and thus evaluate the onset of the M/F interface damage at the mesoscale, an effective M/F interfacial zone damage indicator rate $\dot{\mathcal{D}}_{\mathrm{IZ}}$ is defined. For this, the microscopic damage initiation pattern emerging from extensive interface unit cell numerical simulations (Liu et al., 2021) is used, which showed that when the sliding-triggered interface damage initiation mode dominates, as considered here, the corresponding damage 'hot spot' is typically located in the near-interface ferrite around the RA film tips, as indicated in Fig. 6(a) (see also Fig. 1).

Since microscopic damage often initiates within a zone of finite volume and to eliminate artifacts induced by the numerical discretization, the effective M/F interface damage indicator rate $\dot{\mathcal{D}}_{\mathrm{IZ}}$ is defined as the locally averaged microscopic damage indicator rate $\dot{\mathcal{D}}_{\mathrm{m}}$ within the affected volume of the ferrite matrix around the hot spot:

$$\dot{\mathcal{D}}_{\mathrm{IZ}} \equiv \frac{1}{V^{\mathrm{hs}}_{\mathrm{m,F}}} \int_{\mathcal{V}_{\mathrm{m,F}}} \mathcal{W}_{\mathrm{m}} \dot{\mathcal{D}}_{\mathrm{m}} \, \mathrm{d}V_{\mathrm{m}}, \tag{5}$$

with the affected ferrite volume $V^{\mathrm{hs}}_{\mathrm{m,F}}$ around the hot spot given by

$$V^{\mathrm{hs}}_{\mathrm{m,F}} = \int_{\mathcal{V}_{\mathrm{m,F}}} \mathcal{W}_{\mathrm{m}} \, \mathrm{d}V_{\mathrm{m}}, \tag{6}$$

where the weight function $\mathcal{W}_{\mathrm{m}}$ centered at the hot spot position $\vec{X}^{\mathrm{hs}}_{\mathrm{m}}$ (with 1D sketch shown in Fig. 6(b)) is taken as

$$\mathcal{W}_{\mathrm{m}}(\vec{X}_{\mathrm{m}}) = \cosh^{-2}\left(\frac{\| (\mathbf{I} - \vec{T}_{\mathrm{M/F}} \otimes \vec{T}_{\mathrm{M/F}}) \cdot (\vec{X}_{\mathrm{m}} - \vec{X}^{\mathrm{hs}}_{\mathrm{m}}) \|}{l^{\mathrm{hs}}} \right). \tag{7}$$

Here, $\vec{X}_{\mathrm{m}}$ indicates the position vector of a point in the initial unit cell configuration; $\vec{T}_{\mathrm{M/F}}$ represents a M/F interface tangent in the out-of-plane Z direction; l^{hs} is a hot spot length scale defining the size of $V^{\mathrm{hs}}_{\mathrm{F}}$ and is taken as $l^{\mathrm{hs}} = 2.5$ nm in this study, i.e. sufficiently small compared with the RA film thickness. Note, that the exact location of the hot spot relies on the underlying M/F interface microstructure, which is not resolved at the mesoscale, and is therefore not upscaled.

5. Microscopic unit cell analyses

In this section, several microscopic M/F interfacial zone unit cell simulation results will be presented and analysed to exemplify the relation between the martensite substructure boundary sliding and the interface damage indicator for the subsequent identification of an effective constitutive relation between these two quantities.

The unit cells introduced in Section 3 with the material parameters given in Tables 1 and 2 are analysed. To sample the space of possible sliding directions, a set of simple shear loading cases along the habit plane, which can easily trigger the sliding mode, are defined according to the prescribed mesoscopic deformation gradient tensor

$$\boldsymbol{\mathcal{F}}_{\mathrm{IZ}} = \mathbf{I} + \gamma_{\mathrm{IZ}} \vec{S}^{\mathrm{hp}} \otimes \vec{N}^{\mathrm{hp}}. \tag{8}$$

Here, $\vec{S}^{\mathrm{hp}}$ denotes the shear direction and γ_{IZ} the shear magnitude. A shear direction angle $\psi^{\mathrm{hp}} = \arccos(\vec{S}^{\mathrm{hp}} \cdot \vec{e}_x)$ is introduced, which is measured with respect to the habit plane normal $\vec{N}^{\mathrm{hp}}$, see Fig. 4(a).

First, the unit cell simulations are performed under simple shear with the direction angles $\psi^{\mathrm{hp}} = 90°$ and $\psi^{\mathrm{hp}} = 270°$, i.e. the shear along the positive and negative Z axes, see Fig. 4(a). For these two simple shear cases, the martensite substructure boundary sliding direction is parallel to the RA/F interface, and therefore the RA/F interface orientation and area do not change during the deformation.

The unit cells with different initial RA/F interface orientation angles ranging from $\theta^{\mathrm{hp}} = 0°$ to $\theta^{\mathrm{hp}} = 90°$ are considered. The (accumulated) equivalent plastic strain maps $\varepsilon^{\mathrm{eq}}_{\mathrm{m,p}}$ of three unit cells with $\theta^{\mathrm{hp}} = 90°$, $\theta^{\mathrm{hp}} = 45°$ and $\theta^{\mathrm{hp}} = 0°$, under $\psi^{\mathrm{hp}} = 90°$ simple

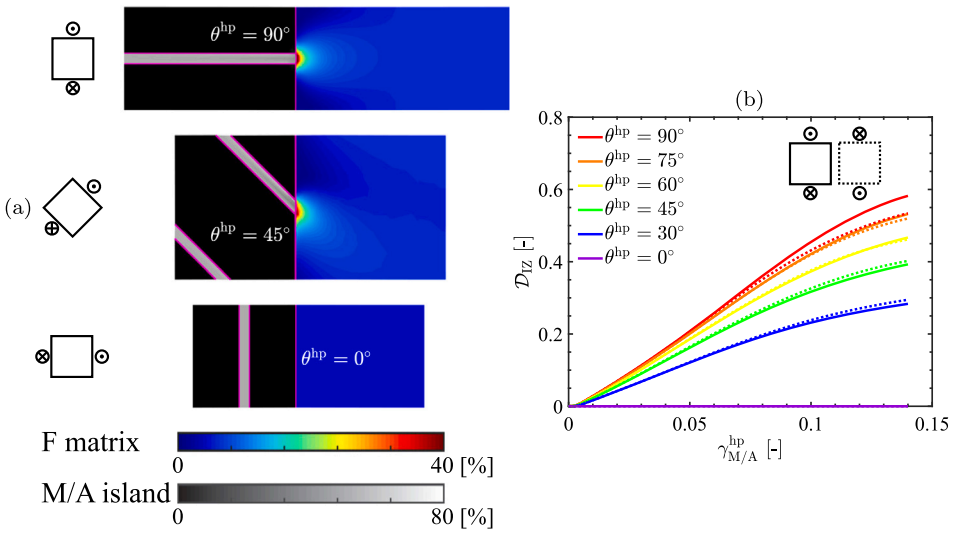

Fig. 7. (a) Equivalent plastic strain maps of three selected microscopic M/F interfacial zone unit cells at an effective sliding magnitude $\gamma^{hp}_{M/A} = 0.1$; (b) effective M/F interface damage indicator versus effective sliding for the six unit cells with different θ^{hp}, under simple shear loading with $\psi^{hp} = 90°$ and $\psi^{hp} = 270°$, indicated by the solid and dashed lines, respectively.

shear, are shown in Fig. 7(a). In all cases, the substructure boundary siding is activated, as evidenced by the high equivalent plastic strain (see light grey) in the RA film . For the $\theta^{hp} = 0°$ case, the RA film does not induce plastic strain concentration in the ferrite matrix. For the other cases, the RA film shearing entails the plastic strain concentrations in the adjacent ferrite. The lower interface orientation angle, e.g. $\theta^{hp} = 45°$, is characterized by the larger initial RA/F interface area, compared to $\theta^{hp} = 90°$, which leads to a more distributed plastic strain concentration for $\theta^{hp} = 45°$.

To quantify the above results in terms of effective quantities, Fig. 7(b) shows the effective sliding magnitude $\gamma^{hp}_{M/A} = \|\vec{\gamma}^{hp}_{M/A}\|$, with $\vec{\gamma}^{hp}_{M/A}$ computed according to Eq. (1) and the effective interface damage indicator $\mathcal{D}_{IZ} = \int \dot{\mathcal{D}}_{IZ}\, dt$, with $\dot{\mathcal{D}}_{IZ}$ obtained according to Eq. (5). In accordance with the observed plastic strain maps, at the same amount of the effective sliding, the effective damage indicator level is highest for the $\theta^{hp} = 90°$ case and reduces for smaller angles, up to zero for the $\theta^{hp} = 0°$ case. This indicates that the initial RA/F interface orientation has a clear influence on the effective interface damage indicator level. This observation will be exploited later in the formulation of the effective interface damage indicator model. In addition, it has been confirmed that in case of sliding parallel to the RA/F interface, considering the stress triaxiality dependent definition for the interface damage indicator does not qualitatively affect the relation between the initial RA/F interface orientation and damage initiation observed from Fig. 7(b).

Moreover, for all θ^{hp} (except for $\theta^{hp} = 0°$), a common trend can be observed in the relation between the effective interface damage indicator and the effective sliding. As the effective sliding increases, the effective interface damage indicator first increases approximately linearly and then tends to saturate at a high sliding level. This saturation is due to the activated lath plasticity, which reduces the plastic strain concentration intensity in the near-interface ferrite. Finally, it is noted that, as expected, the results for the loading directions $\psi^{hp} = 90°$ (see solid lines) and $\psi^{hp} = 270°$ (see dashed lines) are essentially the same, with only a small difference at high sliding levels, which is caused by the near-interface lath plasticity activation, in combination with the minor RA anisotropy in the habit plane.

Next, the unit cell responses for other loading directions, i.e. when the applied shear and the resulting sliding are not parallel to the RA/F interface, are considered. Fig. 8(a) shows the results for the unit cell with the interface orientation angle $\theta^{hp} = 90°$. The damage indicator rates $\dot{\mathcal{D}}_{IZ}$ for different loading directions are plotted normalized by the damage indicator rate averaged for the two loading directions parallel to the RA/F interface, i.e. normalized by $\dot{\mathcal{D}}^{\parallel}_{IZ} = \frac{1}{2}\left(\dot{\mathcal{D}}_{IZ}\big|_{\psi^{hp}=90°} + \dot{\mathcal{D}}_{IZ}\big|_{\psi^{hp}=270°}\right)$, for the unit cell with the same interface orientation. The normalized effective damage indicator rates are approximately symmetric about the Z axis, because of the symmetry of the $\theta^{hp} = 90°$ unit cell geometry with respect to the habit plane. This symmetry can also be observed in the equivalent plastic strain maps, which are mirrored about the habit plane for $\psi^{hp} = 0°$ and $\psi^{hp} = 180°$.

The results for the unit cell with $\theta^{hp} = 45°$ are shown in Fig. 8(b). The pattern of the normalized effective damage indicator rate is strongly anisotropic, reflecting the asymmetry of the unit cell geometry. Indeed, the equivalent plastic strain maps differ significantly for $\psi^{hp} = 0°$ and $\psi^{hp} = 180°$, where the latter shows a higher plastic strain concentration intensity in the near-interface ferrite. This may originate from the formation of a sharper RA/F film tip for the $\psi^{hp} = 180°$ case compared to the $\psi^{hp} = 0°$ case. Clear dependency on the sliding direction implies that the effective interface damage indicator is in general affected by the RA/F interface orientation change during the deformation. The results for other unit cells with $\theta^{hp} \neq 90°$ confirm similar features to those presented for $\theta^{hp} = 45°$ and are therefore not shown here. In addition, it has been confirmed that for each θ^{hp}, including the stress triaxiality in the interface damage indicator definition does not qualitatively affect the dependency on the sliding direction observed from Fig. 8.

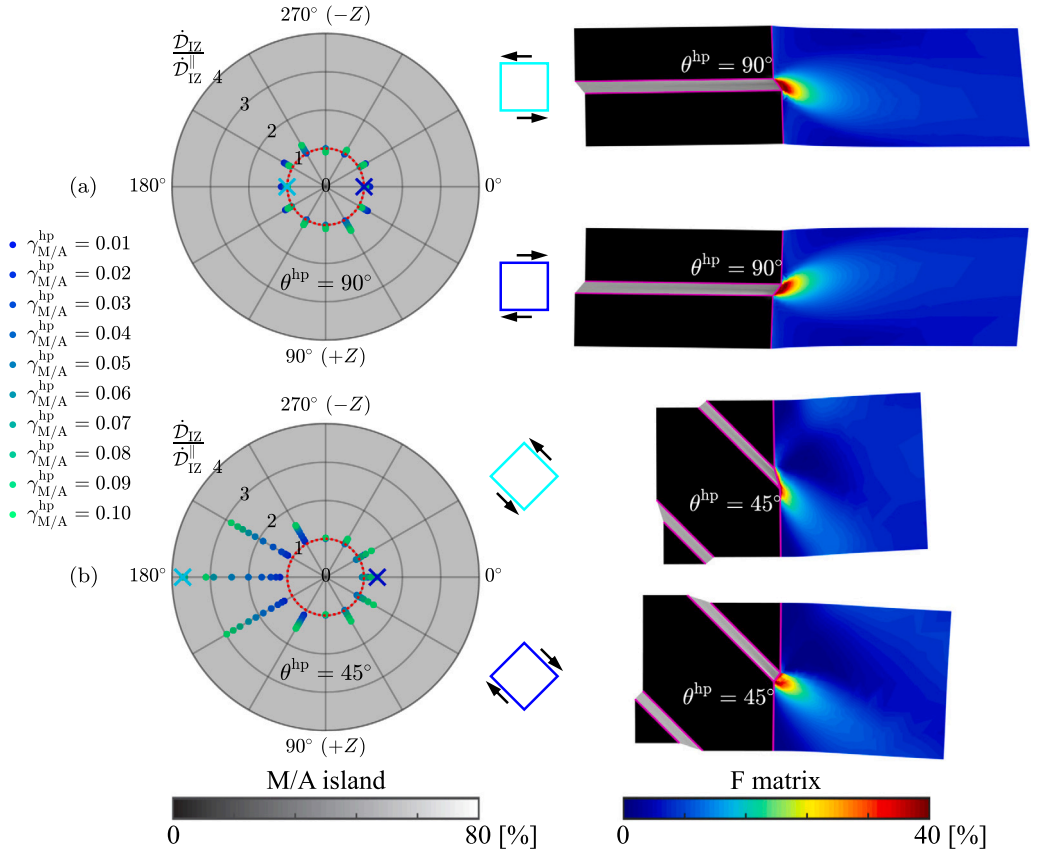

Fig. 8. Normalized effective M/F interface damage indicator rates for different applied simple shear loading directions ψ^{hp}, plotted in a polar coordinate system, and the equivalent plastic strain maps for two selected simple shear loading directions $\psi^{hp} = 0°$ and $\psi^{hp} = 180°$, at an effective sliding magnitude $\gamma^{hp}_{M/A} = 0.1$, for the two microscopic M/F interfacial zone unit cells: (a) $\theta^{hp} = 90°$ and (b) $\theta^{hp} = 45°$. For reference, the red circles represent $\dot{\mathcal{D}}_{IZ}/\dot{\mathcal{D}}^{\parallel}_{IZ} = 1$.

6. Constitutive model relating the effective interface damage indicator and sliding

6.1. Effective constitutive model formulation

Microscale unit cell simulations indicate a relationship between the effective quantities defined in Section 4, i.e. the effective interface damage indicator and the effective sliding of the martensite island. However, considering the large variation in local M/F interface orientations with respect to the habit plane and (local) loading conditions, performing unit cell computations for all possible cases (either 'on the fly' or on beforehand) would be computationally extremely expensive, impractical and virtually infeasible. Therefore, here an effective constitutive model that relates the interface damage indicator and the sliding as a function of geometrical parameters will de developed.

To this aim, consistent with the assumption that the martensite substructure boundary sliding dominates the damage initiation in the M/F interfacial zone, the damage indicator rate is first computed for a unit cell with a selected, reference interface orientation angle θ^{hp}_{r}, and correlated to the resulting effective sliding $\vec{\gamma}^{hp}_{M/A}$ of the martensite island. This provides the reference damage indicator rate $\dot{\mathcal{D}}^{r}_{IZ}(\vec{\gamma}^{hp}_{M/A}; \theta^{hp}_{r})$. The choice of the reference orientation is arbitrary, but to provide meaningful results the considered orientation should activate a noticeable amount of sliding under the applied loading.

Next, in accordance with the definition of the effective interface damage indicator as a quantity in the near-interface ferrite around the RA film tip (see Section 4) and the unit cell analyses (see Section 5), two geometrical parameters can be identified that significantly affect the damage indicator rate:

- The geometrical orientation of the RA film (and thus the martensite lath) with respect to the M/F interface in the undeformed state; assuming the same RA film thickness for all unit cells with different interface orientations, this translates to the RA/F interface area.
- The change of the orientation of the RA/F interface due to the deformation, which can also be accompanied by a change of the area.

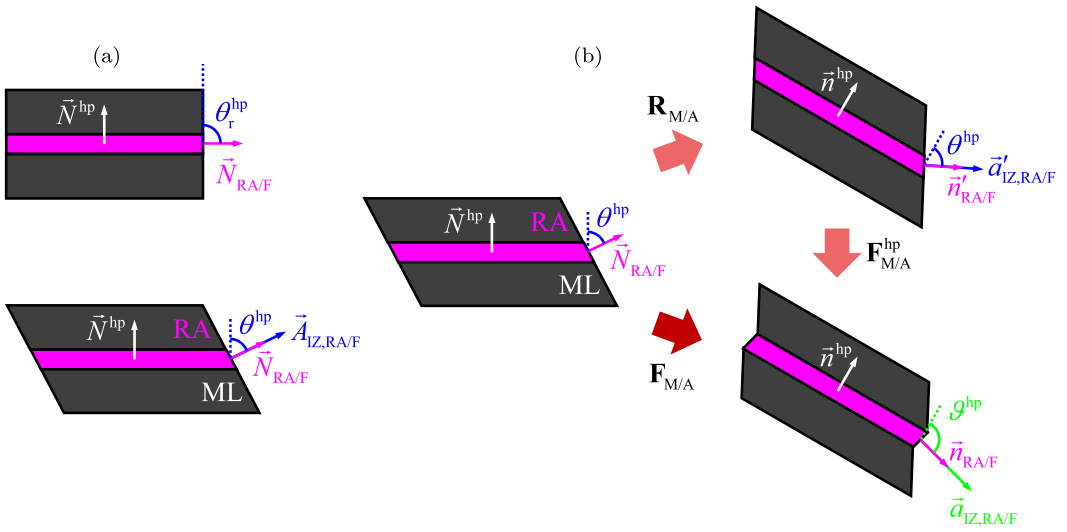

Fig. 9. 2D sketches of (a) the reference microscopic M/F interfacial zone unit cell with θ_r^{hp} and a unit cell with an arbitrary θ^{hp}, and (b) the initial undeformed, rigid-body rotated and current deformed configurations of a unit cell. The ferrite matrix is not displayed and the thickness of the RA film is exaggerated for clarity.

The first geometrical parameter can be represented by the ratio between the RA film area adjacent to the ferrite in the unit cell with the reference interface orientation angle θ_r^{hp} to the one of an arbitrary interface orientation angle θ^{hp}. Assuming the same RA film thickness, this parameter can be defined as:

$$f_{IZ}^{A}(\theta^{hp},\theta_r^{hp}) \equiv \frac{\|\vec{A}_{IZ,RA/F}(\theta_r^{hp})\|}{\|\vec{A}_{IZ,RA/F}(\theta^{hp})\|} = \frac{\sin(\theta^{hp})}{\sin(\theta_r^{hp})}, \tag{9}$$

with $\vec{A}_{IZ,RA/F}$ the oriented area in the initial configuration where the RA film and F matrix contact each other within the unit cell for either θ_r^{hp} or θ^{hp}, see Fig. 9(a).

The second geometrical parameter describing the effect of the change of the orientation and area of the RA/F interface as a result of the deformation (and thus also as a result of the effective sliding $\vec{\gamma}_{M/A}^{hp}$) for a unit cell with θ^{hp} is defined as:

$$\begin{aligned} c_{IZ}^{A}(\vec{\gamma}_{M/A}^{hp};\theta^{hp}) &\equiv \frac{|\vec{a}_{IZ,RA/F}(\vec{\gamma}_{M/A}^{hp};\theta^{hp})\cdot\vec{a}'_{IZ,RA/F}(\theta^{hp})|}{\|\vec{a}'_{IZ,RA/F}(\theta^{hp})\|^2} - 1 \\ &= \left|\cos\left(\vartheta^{hp}(\vec{\gamma}_{M/A}^{hp}) - \theta^{hp}\right)\right| \frac{\sin(\theta^{hp})}{\sin\left(\vartheta^{hp}(\vec{\gamma}_{M/A}^{hp})\right)} - 1, \end{aligned} \tag{10}$$

where $\vec{a}'_{IZ,RA/F}$ and $\vec{a}_{IZ,RA/F}$ are the oriented RA/F interface areas in the rigid-body rotated and deformed configurations, respectively, see Fig. 9(b). To obtain the second equality in Eq. (10), the geometrical relations shown in Fig. 9(b) have been used with

$$\vartheta^{hp} = \arccos(\vec{n}_{RA/F}\cdot\vec{n}^{hp}), \tag{11}$$

where the current habit plane normal $\vec{n}^{hp}$ can be determined using Eq. (3). Assuming fully plastic deformation of the RA film, i.e. neglecting the elastic volume change, the current RA/F interface normal $\vec{n}_{RA/F}$ is obtained by Nanson's formula as

$$\vec{n}_{RA/F} = \vec{N}_{RA/F}\cdot\mathbf{F}_{RA}^{-1}, \tag{12}$$

with the (sliding-induced) RA film deformation gradient tensor $\mathbf{F}_{RA}$ expressed in terms of the effective sliding $\vec{\gamma}_{M/A}^{hp}$ (measured in the rotated configuration, see Fig. 5) of the martensite island as

$$\mathbf{F}_{RA} = \left(\mathbf{I} + \frac{\eta_{M/A}}{\eta_{RA}}\vec{\gamma}_{M/A}^{hp}\otimes\vec{n}^{hp}\right)\cdot\mathbf{R}_{M/A}, \tag{13}$$

where $\mathbf{R}_{M/A}$ denotes the martensite island rigid-body rotation with respect to the initial configuration, i.e. $\mathbf{F}_{M/A} = \mathbf{F}_{M/A}^{hp}\cdot\mathbf{R}_{M/A}$ with $\mathbf{F}_{M/A}^{hp} = \mathbf{I} + \vec{\gamma}_{M/A}^{hp}\otimes\vec{n}^{hp}$ the martensite sliding deformation gradient tensor with respect to the rigid-body rotated configuration, see Fig. 5; the volume fraction ratio $\eta_{RA}/\eta_{M/A}$ physically represents the RA volume fraction within the martensite and thus directly relates $\mathbf{F}_{M/A}$ to $\mathbf{F}_{RA}$ under the assumption of negligible lath plastic deformation.

With the above definitions, a mesoscale constitutive model relating the time evolution of the effective interface damage indicator $\mathcal{D}_{\mathrm{IZ}}$ and sliding $\vec{\gamma}^{\mathrm{hp}}_{\mathrm{M/A}}$ can be proposed in the following form:

$$\begin{aligned}\mathcal{D}_{\mathrm{IZ}} &= \mathfrak{D}_{\mathrm{IZ}}(\vec{\gamma}^{\mathrm{hp}}_{\mathrm{M/A}};\theta^{\mathrm{hp}},\theta^{\mathrm{hp}}_{\mathrm{r}}) \\ &= \int \mathcal{M}_2\left(c^{A}_{\mathrm{IZ}}(\vec{\gamma}^{\mathrm{hp}}_{\mathrm{M/A}};\theta^{\mathrm{hp}})\right)\,\mathcal{M}_1\left(f^{A}_{\mathrm{IZ}}(\theta^{\mathrm{hp}},\theta^{\mathrm{hp}}_{\mathrm{r}})\right)\,\dot{\mathcal{D}}^{\mathrm{r}}_{\mathrm{IZ}}(\vec{\gamma}^{\mathrm{hp}}_{\mathrm{M/A}};\theta^{\mathrm{hp}}_{\mathrm{r}})\,\mathrm{d}t,\end{aligned} \tag{14}$$

consisting of a reference damage indicator $\mathcal{D}^{\mathrm{r}}_{\mathrm{IZ}}$ corrected by two geometrical influence functions $\mathcal{M}_1$ and $\mathcal{M}_2$, which quantify the influence of the initial interface orientation (measured by a ratio f_{IZ}) and the interface orientation change (measured by a ratio change c_{IZ}) during the deformation, respectively. The proposed multiplicative decomposition into $\mathcal{M}_1$ and $\mathcal{M}_2$ is confirmed able to sufficiently reproduce the data obtained from all unit cell simulations, as to be demonstrated in the following.

For the characterization of this constitutive relation (14), several off-line unit cell pre-computations should be performed. First, the reference damage indicator rate $\dot{\mathcal{D}}^{\mathrm{r}}_{\mathrm{IZ}}(\vec{\gamma}^{\mathrm{hp}}_{\mathrm{M/A}};\theta^{\mathrm{hp}}_{\mathrm{r}})$ as a function of the sliding activity $\vec{\gamma}^{\mathrm{hp}}_{\mathrm{M/A}}$ will be extracted from a single reference unit cell simulation with the interface orientation angle $\theta^{\mathrm{hp}}_{\mathrm{r}}$ and subjected to a loading condition which does not induce a RA/F interface orientation change. Next, the two geometrical influence functions $\mathcal{M}_1\left(f^{A}_{\mathrm{IZ}}(\theta^{\mathrm{hp}},\theta^{\mathrm{hp}}_{\mathrm{r}})\right)$ and $\mathcal{M}_2\left(c^{A}_{\mathrm{IZ}}(\vec{\gamma}^{\mathrm{hp}}_{\mathrm{M/A}};\theta^{\mathrm{hp}})\right)$ will be identified from the results of several representative unit cell simulations with different θ^{hp} and loading conditions. This process will be elaborated and illustrated subsequently.

6.2. Identification of the effective constitutive model

To identify the functional form and parameters describing the mesoscale constitutive relation between the effective M/F interface damage indicator and effective substructure boundary sliding of the martensite island, the results of the unit cell simulations with different interface orientations and shear loading directions as presented in Section 5 will be used.

As the reference simulation, the unit cell with $\theta^{\mathrm{hp}}_{\mathrm{r}} = 90°$ loaded in the shear directions $\psi^{\mathrm{hp}} = 90°$ and $\psi^{\mathrm{hp}} = 270°$ is selected. This choice is motivated by the fact that this case exhibits pronounced martensite island sliding interacting with the ferrite matrix, see Fig. 7(a). In this study, the reference damage indicator rate is therefore obtained as

$$\dot{\mathcal{D}}^{\mathrm{r}}_{\mathrm{IZ}}(\vec{\gamma}^{\mathrm{hp}}_{\mathrm{M/A}}) = \tfrac{1}{2}\left(\dot{\mathcal{D}}_{\mathrm{IZ}}(\vec{\gamma}^{\mathrm{hp}}_{\mathrm{M/A}})\Big|_{\theta^{\mathrm{hp}}_{\mathrm{r}}=90°;\psi^{\mathrm{hp}}=90°} + \dot{\mathcal{D}}_{\mathrm{IZ}}(\vec{\gamma}^{\mathrm{hp}}_{\mathrm{M/A}})|_{\theta^{\mathrm{hp}}_{\mathrm{r}}=90°;\psi^{\mathrm{hp}}=270°}\right). \tag{15}$$

Next, the function $\mathcal{M}_1\left(f^{A}_{\mathrm{IZ}}(\theta^{\mathrm{hp}},\theta^{\mathrm{hp}}_{\mathrm{r}})\right)$ is identified. The unit cell simulations in Section 5 indicate that in absence of a RA/F interface orientation change, for all values of the effective sliding $\vec{\gamma}^{\mathrm{hp}}_{\mathrm{M/A}}$, the effective interface damage indicator is lower for smaller interface orientation angles θ^{hp}, see Fig. 7(b). For the selected reference interface orientation angle, $\theta^{\mathrm{hp}}_{\mathrm{r}} = 90°$, smaller interface orientation angles correspond to smaller values of the parameter $f^{A}_{\mathrm{IZ}}(\theta^{\mathrm{hp}},\theta^{\mathrm{hp}}_{\mathrm{r}})$ characterizing the RA/F interface area in the initial, undeformed configuration, as defined in Eq. (9). Indeed, plotting the normalized damage indicator rates $\dot{\mathcal{D}}_{\mathrm{IZ}}/\dot{\mathcal{D}}^{\mathrm{r}}_{\mathrm{IZ}}$ for all considered θ^{hp} and at different levels of $\vec{\gamma}^{\mathrm{hp}}_{\mathrm{M/A}}$ in Fig. 10(a), reveals a linear relation with respect to f^{A}_{IZ}, the proportionality coefficient of which equals 1 on average. Therefore, for simplicity it can be assumed that

$$\mathcal{M}_1\left(f^{A}_{\mathrm{IZ}}(\theta^{\mathrm{hp}},\theta^{\mathrm{hp}}_{\mathrm{r}})\right) = f^{A}_{\mathrm{IZ}}(\theta^{\mathrm{hp}},\theta^{\mathrm{hp}}_{\mathrm{r}}) = \frac{\sin(\theta^{\mathrm{hp}})}{\sin(\theta^{\mathrm{hp}}_{\mathrm{r}})}. \tag{16}$$

Note, that this expression for $\mathcal{M}_1$ does not introduce any additional parameters. Substituting the expression (16) for $\mathcal{M}_1$ together with $\dot{\mathcal{D}}^{\mathrm{r}}_{\mathrm{IZ}}$ given by Eq. (15) into Eq. (14) and disregarding for the moment the term $\mathcal{M}_2$, provides the resulting damage indicator $\mathcal{D}_{\mathrm{IZ}}$ as shown in Fig. 10(b). The prediction compares well with the fully resolved unit cell simulation results, with a relative deviation within approximately 5%.

Finally, to identify the function $\mathcal{M}_2\left(c^{A}_{\mathrm{IZ}}(\vec{\gamma}^{\mathrm{hp}}_{\mathrm{M/A}};\theta^{\mathrm{hp}})\right)$, the normalized damage indicator rate $\dot{\mathcal{D}}_{\mathrm{IZ}}/(\mathcal{M}_1\dot{\mathcal{D}}^{\mathrm{r}}_{\mathrm{IZ}})$ for all considered θ^{hp} and different sliding directions has been plotted in Fig. 11 against the RA/F interface oriented area change c^{A}_{IZ}, defined in (10). To capture the data trends observed in Fig. 11, the following expression for $\mathcal{M}_2$ is adopted

$$\mathcal{M}_2\left(c^{A}_{\mathrm{IZ}}(\vec{\gamma}^{\mathrm{hp}}_{\mathrm{M/A}};\theta^{\mathrm{hp}})\right) = k|c^{A}_{\mathrm{IZ}} - c_0|^{p} + 1, \tag{17}$$

where k, c_0 and p are three parameters. The parameter identification with $k = 7.21$, $c_0 = -0.140$ and $p = 2.28$ is shown in Fig. 11 and adequately reproduces most data obtained from different unit cells at different sliding levels. The data spread in the unit cell simulation results can be attributed to the activation of the out-of-habit-plane slip systems in the RA films in some cases and to the near-interface lath plasticity activation, especially at higher strain levels. This out-of-habit-plane contribution is, however, not included in the present effective constitutive model.

To demonstrate the predictive capabilities of the identified effective constitutive model, the effective interface damage indicators $\mathcal{D}_{\mathrm{IZ}}$ computed according to Eq. (14), with Eqs. (15), (16) and (17), as a function of the effective sliding $\vec{\gamma}^{\mathrm{hp}}_{\mathrm{M/A}}$ are plotted in Fig. 12 and compared to the results of the fully resolved unit cell simulations for several interface orientation angles θ^{hp}. In order to visualize the sliding direction dependency (see Fig. 8), the effective sliding magnitude has been given a sign in accordance with the direction angle ψ^{hp} of the applied loading:

$$\bar{\gamma}^{\mathrm{hp}}_{\mathrm{M/A}} = \begin{cases} -\gamma^{\mathrm{hp}}_{\mathrm{M/A}}, & \text{if } 90° < \psi^{\mathrm{hp}} \le 270° \\ +\gamma^{\mathrm{hp}}_{\mathrm{M/A}}, & \text{otherwise.} \end{cases} \tag{18}$$

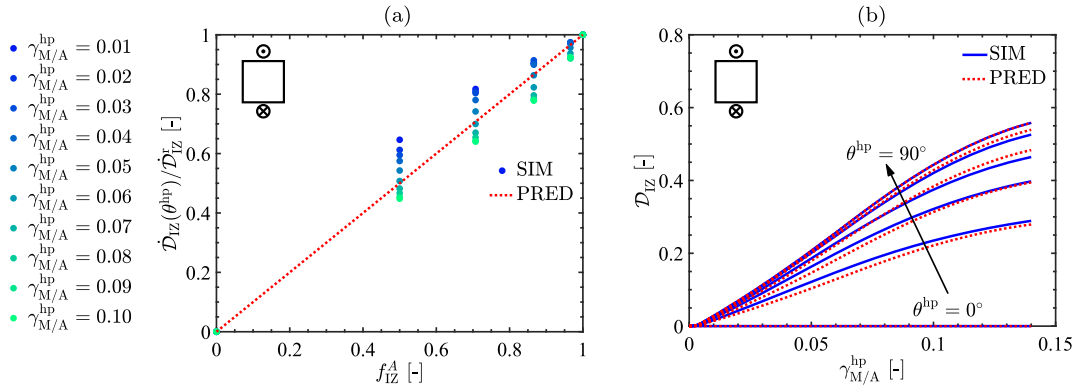

Fig. 10. Comparison between the microscopic M/F interfacial zone unit cell simulation results (SIM) with different θ^{hp}, in case of the sliding direction parallel to the RA/F interface, and the prediction (PRED) using the effective constitutive model: (a) normalized effective M/F interface damage indicator rate for all considered θ^{hp} relative to the reference $\theta^{hp}_{r} = 90°$ versus the initial RA/F interface area ratio; (b) effective M/F interface damage indicator versus effective sliding.

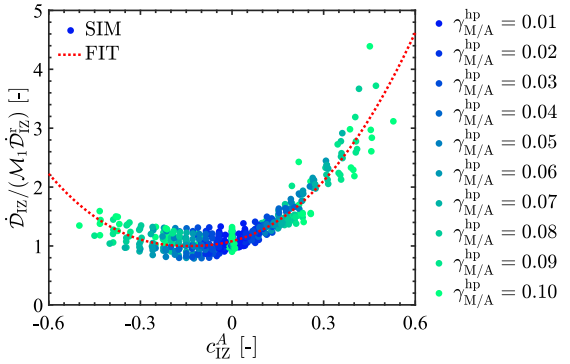

Fig. 11. Normalized effective M/F interface damage indicator rate versus the RA/F interface oriented area change for the microscopic M/F interfacial zone unit cells with different θ^{hp}. Comparison between the unit cell simulation results (SIM) and the model fit (FIT).

To expose the dependency of the effective interface damage indicator on the sliding direction, for each value of the signed effective sliding magnitude, the average and standard deviation band of the damage indicators obtained for different loading direction angles ψ^{hp} are shown, for both, the unit cell simulations and the effective constitutive model prediction. The effective model predictions adequately capture the fully resolved unit cell simulation results, with small deviations that can be attributed to the out-of-habit-plane slip which is not included in the proposed effective constitutive model. The interface orientation direction dependent asymmetry of the damage indicator pattern with respect to the sliding direction is also well reproduced by the effective model. As expected, for the $\theta^{hp} = 90°$ case, the damage indicator pattern is symmetric with respect to the loading direction. As the initial RA interface orientation angle θ^{hp} decreases, the asymmetry first increases and then decreases, since the RA/F interface tends to become parallel to the habit plane, in which case the RA/F interface orientation change effect gradually becomes negligible.

It has been verified that within the sliding-dominated M/F interface deformation regimes, the geometrical influence functions (16) and (17) identified above are also applicable for a broad range of phase contrasts (even when a different ferrite material model is used), implying the generality of the developed effective interface damage indicator model (14).

7. M/F interface damage initiation analysis in a DP steel mesostructure

In this section, the application potential of the effective M/F interface damage indicator model presented above will be demonstrated on a realistic DP steel mesostructure containing several lath martensite islands.

7.1. Mesoscopic simulation setup

The in-plane DP steel mesostructure geometry, shown in Fig. 13, is obtained using optical microscopy (Maresca et al., 2016a), and has dimensions 66.9 μm×50.7 μm with a 34.2% martensite volume fraction. The martensite lath and RA film thicknesses are taken as 90 nm and 10 nm, respectively, resulting in a RA volume fraction of 10% within each martensite island. For each mesostructure realization, a random BCC crystallographic orientation was assigned to each martensite island, i.e. all the laths in a martensite island (see Fig. 13(a) for an example). The FCC crystallographic orientations of the RA films and hence the martensite habit plane normals

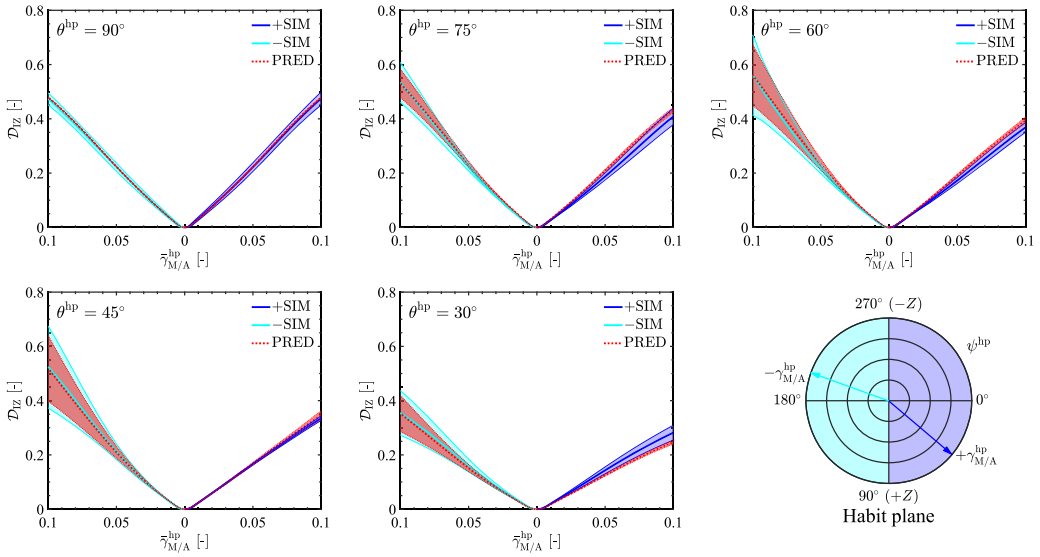

Fig. 12. Comparison between the microscopic M/F interfacial zone unit cell simulation results (SIM) and the prediction (PRED) using the effective constitutive model: effective M/F interface damage indicator versus effective sliding, for the five unit cells with different θ^{hp}, under simple shear loading with different ψ^{hp}. The defined negative and positive sliding directions are depicted on the habit plane, in cyan and blue, respectively.

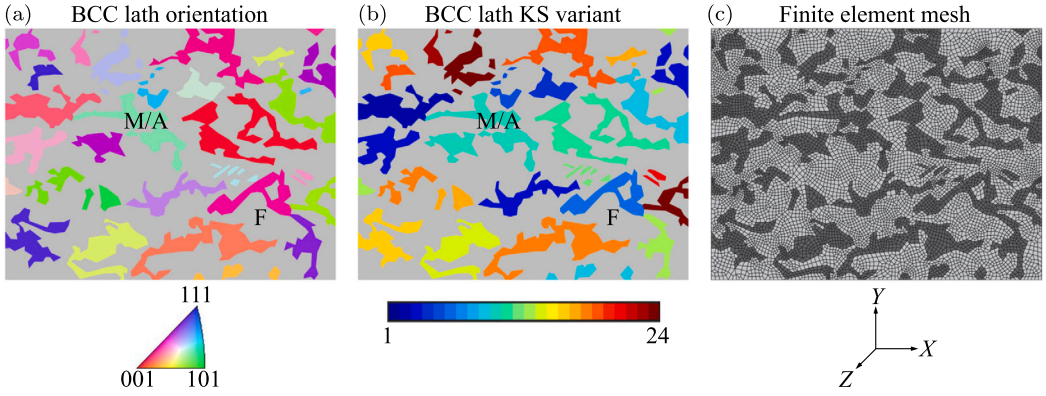

Fig. 13. DP steel mesoscale model for the random realization "RR-1": (a) the BCC crystallographic orientation map of the martensite laths within the martensite islands and (b) the KS variant index map determining the FCC crystallographic orientations of the RA films, and (c) the corresponding in-plane finite element mesh.

$\vec{N}^{hp}$ within each martensite island have been obtained by randomly assigning a KS variant index to the BCC lath (see Fig. 13(b) for an example), numbered according to the variant list in Morito et al. (2003). Using $\vec{N}^{hp}$ together with the local RA/F interface normal $\vec{N}_{RA/F}$ (= $\vec{N}_{M/F}$), the local angle θ^{hp} between the RA/F interface (or the M/F interface) and the habit plane has been determined. To account for the mesostructural variability, five different random realizations (RR) of the BCC lath crystallographic orientations and FCC RA film crystallographic orientations determined according to the KS variant indexes have been considered.

For consistency with the microscopic M/F interfacial zone unit cell simulations, from which the effective interface damage indicator model has been identified, the ferrite matrix in the DP steel mesoscale model is also modelled with the isotropic elasto-plasticity (see Appendix B.2) with the material parameters given in Table 2.

For the modelling of the martensite islands with embedded thin RA films, the direct discretization of the microscale laths and RA films would be practically infeasible due to the large difference in the sizes between the meso- and micro-scales. To this end, in order to capture the favourable sliding-induced deformation mode of the martensite island at reasonable computational costs, a reduced lath martensite model is adopted here. In this model, the martensite substructure (more generally, (sub-)blocks) is modelled implicitly such that there is no need to spatially resolve the laths and RA films. Instead, the substructure is described with a multi-scale lamella model representing the stack of martensite laths and RA films complying traction equilibrium and deformation compatibility at the M/RA interface (Maresca et al., 2014b). At the same time, to reduce the computational costs even more, the FCC RA film and BCC lath models are further simplified. For the RA films, a reduced crystal plasticity model is used (Maresca et al., 2016b), where only the slip on the three FCC slip systems parallel to the habit plane are explicitly resolved. The plastic deformation

Table 3
Material parameters of the isotropic contribution in the reduced martensite island model.

Parameter	Symbol	Lath	RA film
Reference strain rate	$\dot{\varepsilon}_0$	0.01 [s^{-1}]	0.01 [s^{-1}]
Initial yield stress	M_0	2.257 [GPa]	0.814 [GPa]
Saturation yield stress	M_∞	8.850 [GPa]	1.044 [GPa]
Reference hardening modulus	H_0	24.76 [GPa]	2.992 [GPa]
Strain rate sensitivity	a	0.05 [–]	0.05 [–]
Hardening exponent	b	1.5	1.5

in other directions is modelled by a von Mises-like (visco-)plastic flow rule, projected onto the space orthogonal to the space of the three resolved slip systems. This model is briefly summarized in Appendix C, and more details can be found in Maresca et al. (2016b). Furthermore, in accordance with the observation that the plastic deformation of the laths is usually limited, the material behaviour of the laths is modelled by isotropic (visco-)plasticity.

The material parameters for the isotropic contribution in the RA film model and the isotropic lath model are listed in Table 3. These parameters have been identified from the crystal plasticity model parameters in Table 1, by accounting for a Taylor factor $\mathcal{T} = 3.07$ (Rosenberg and Piehler, 1971) and a latent/self hardening ratio $q = 1.4$ for the FCC RA films (with one slip family) and $\mathcal{T} = 2.95$ (Rosenberg and Piehler, 1971) and $q = 1.4$ for the BCC laths considering two slip families. More details on the parameter identification for the reduced martensite island model can be found in Appendix C.3. The material parameters for the three explicitly resolved FCC slip systems are the same as those listed in Table 1.

The reduced martensite island model is implemented using a user-defined subroutine HYPELA2.F, supported in the commercial FEM package MSC.MARC.

The DP steel mesostructure is discretized using 3D linear finite elements with one element in the out-of-plane direction and the average in-plane element size is ∼0.6 μm. The resulting finite element mesh is shown in Fig. 13(c). Periodic boundary conditions are enforced on the mesostructure boundaries in all three spatial directions. In-plane biaxial loading (representing the pure shear case with a shear direction 45°) is imposed on the considered DP steel mesoscale model, given by the overall deformation gradient tensor $\langle \mathbf{F} \rangle = \lambda \vec{e}_x \otimes \vec{e}_x + \frac{1}{\lambda} \vec{e}_y \otimes \vec{e}_y + \vec{e}_z \otimes \vec{e}_z$, with λ denoting the prescribed stretch ratio along the X axis.

7.2. Overall stress–strain response analysis

Fig. 14(a) reports the overall equivalent von Mises stress $\langle \sigma \rangle^{\mathrm{eq}}$ versus the applied overall equivalent strain $\langle \varepsilon \rangle^{\mathrm{eq}}$ of the considered DP steel mesostructure for five random realizations of the martensite island orientations. The average behaviour of the individual phases, i.e. the martensite islands and the ferrite matrix, is also shown in Fig. 14(a). Here, $\langle \bullet \rangle$ denotes the volume average over the respective domain, i.e. the whole modelled DP steel mesostructure, the martensite islands or the ferrite matrix. Note, that the overall responses of the ferrite matrix in all considered models are similar due to the use of the isotropic elasto-plastic material model for ferrite, which has only a minor effect on the results here. The overall responses of the martensite islands, on the other hand, differ for different realizations. However, a common feature can be observed, namely the apparent continuous yielding behaviour which starts at stress levels below 2 GPa, lower than the BCC lath yield stress. As a result, the overall stress response of the whole DP steel mesostructure demonstrates a well-known continuous yielding feature, without a clear yielding point (see e.g. Mazinani and Poole, 2007). To rationalize these observations, the volume-averaged stress–strain curve of each martensite island for the random realization "RR-1" is plotted in Fig. 14(b). The results for the other random realizations show similar behaviour and are therefore not shown here. The stress–strain responses of different martensite islands are very heterogeneous. Interestingly, only a limited number of martensite islands show large overall strain, however most of the islands have an apparent yield stress below 2 GPa, i.e. lower than the BCC lath yield stress. These results indicate that the substructure boundary sliding is indeed the favourable deformation mode for the martensite islands upon mesoscopic mechanical loading, thus once more confirming the key hypothesis adopted for the proposed multi-scale framework (see Section 2).

7.3. Mesoscopic interface damage initiation analysis

Next, the M/F interface damage initiation in the considered DP mesoscale models is analysed using the developed effective interface damage indicator model (14). The effective sliding $\vec{\gamma}^{\mathrm{hp}}_{\mathrm{M/A}}$ in each martensite island is determined by substituting the deformation gradient tensor $\mathbf{F}_{\mathrm{M/A}}$ at each (integration) point into Eq. (2). The M/F interface damage indicator $\mathcal{D}_{\mathrm{IZ}}$ at each mesoscopic M/F interface point can then be evaluated by substituting $\vec{\gamma}^{\mathrm{hp}}_{\mathrm{M/A}}$ of the near-interface martensite, i.e. the martensite finite element attached to the M/F interface, into Eq. (14). The maps of the effective sliding $\gamma^{\mathrm{hp}}_{\mathrm{M/A}}$ together with the resulting damage indicators $\mathcal{D}_{\mathrm{IZ}}$ for three realizations, "RR-1", "RR-4" and "RR-5", are reported in Fig. 15(a). The other random realization models show similar features and are therefore not presented here. It can be observed, that the majority of interface damage 'hot spots' are located around the martensite islands with a higher magnitude of effective sliding, see Fig. 15(a). Notice, however, that using the effective sliding only is not sufficient to predict the exact locations of the interface damage hot spots, which are also strongly dependent on the interface orientation with respect to the habit plane (i.e. the angle θ^{hp}), as implied in Eq. (14) and confirmed by the mesoscopic simulation results. Fig. 15(b) shows the maps of the equivalent plastic strain $\varepsilon^{\mathrm{eq}}_{\mathrm{p}}$ in the ferrite matrix and martensite

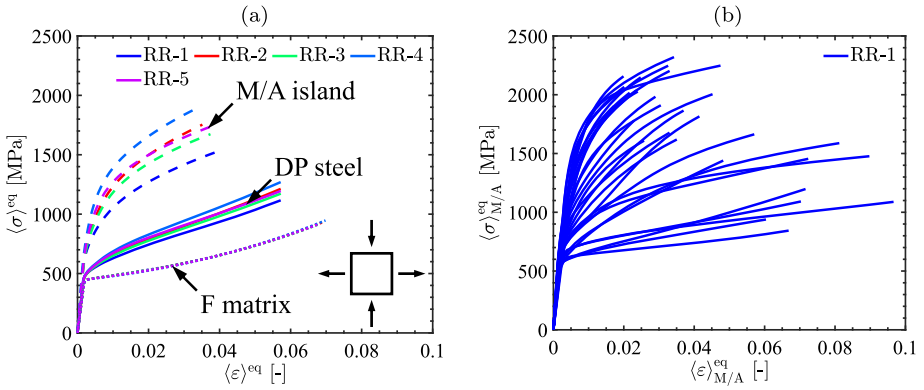

Fig. 14. (a) Equivalent overall stress versus strain of the considered DP steel mesostructure for five random realizations of the BCC lath crystallographic orientations and KS variant indexes, under the biaxial loading; (b) equivalent stress versus strain of each martensite island for the random realization "RR-1".

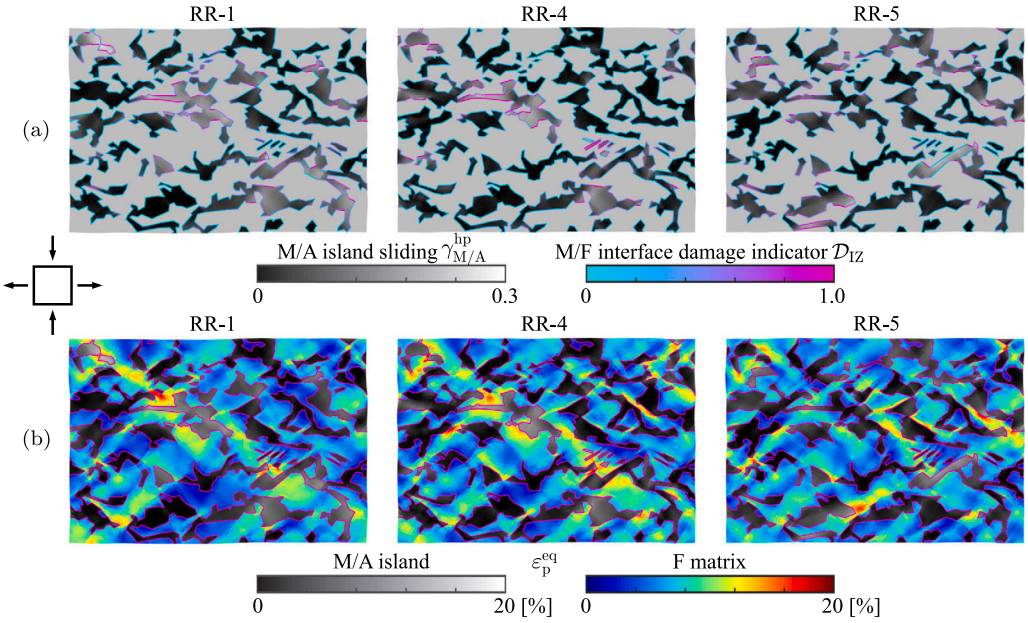

Fig. 15. (a) Martensite island sliding maps and the corresponding M/F interface damage indicators, and (b) equivalent plastic strain maps of the considered DP steel mesostructures for three selected random realizations of the BCC lath crystallographic orientations and KS variant indexes, under biaxial loading, at a prescribed overall equivalent strain $\langle\varepsilon\rangle^{\mathrm{eq}} = 5.75\%$.

islands. Even though many plastic bands in ferrite are oriented at ~45°, dictated by the biaxial loading, the ferrite matrix plasticity is clearly influenced by the local martensite island morphology, but also by the sliding activity of the martensite island. Another important observation is that due to the substructure boundary sliding mechanism, local strain levels of many martensite islands are comparable to those of the ferrite matrix, corresponding to a weak M/F strain partitioning, as observed in experiments (see e.g. Kang et al., 2007; Ghadbeigi et al., 2010; Kamikawa et al., 2015).

8. Conclusions

This contribution presented a multi-scale framework to predict the damage initiation at M/F interfaces in DP steel mesostructures. The DP steel mesostructure consists of multiple lath martensite islands embedded in a ferrite matrix, with M/F interfaces in between. At the microscale, a M/F interfacial zone unit cell is considered, which resolves in detail the martensite substructure consisting of martensite laths with RA films. The sliding of this martensite substructure has been shown to be the dominating deformation mode at the microscale, which triggers the onset of damage in the near-interface ferrite, accompanied by a microscopic damage initiation pattern. Based on these observations, the effective governing quantities, i.e. the sliding of the martensite island and the interface damage indicator, have been defined and upscaled to the mesoscale, through a rigorous scale-bridging scheme. By correlating these

two effective quantities over a large range of interface orientations, sliding directions and phase contrasts, an effective interface damage indicator model as a function of the sliding activity has been obtained. The model takes into account the effect of the initial interface orientation and the interface orientation change as a result of the deformation. This microphysics-based M/F interface damage indicator model, which could not be envisioned a-priori, needs to be identified only once using a set of off-line representative microscopic M/F interfacial zone unit cell simulations and then transferred to the mesoscale. An application of the formulated model after parameter identification has been demonstrated on a realistic DP steel mesostructure. The importance of including the interface orientation for determining locations of the mesoscopic M/F interface damage hot spots is especially emphasized.

In the future, the modelling framework can be extended to include the effects of the ferrite grain orientation, carbon distribution and possible near-interface precipitates. Besides, other choices of the microscopic damage indicator model form, e.g. those further incorporating the stress triaxiality and Lode angle, will be investigated in details. Moreover, quantitative model validation at both microscale and mesoscale will be conducted in a systematic manner.

To conclude, the proposed multi-scale framework enables efficient, microphysics-based prediction of the M/F interface damage initiation in DP steel mesostructures, which was not possible with available "traditional" approaches, thereby providing a powerful tool to assess ductility, identify critical damage-related microstructural features, and provide design guidelines for new generation of advanced high strength steels.

CRediT authorship contribution statement

L. Liu: Methodology, Software, Visualization, Writing – original draft. **F. Maresca:** Conceptualization, Writing – review & editing, Supervision. **J.P.M. Hoefnagels:** Conceptualization, Investigation, Writing – review & editing. **M.G.D. Geers:** Conceptualization, Writing – review & editing, Supervision, Funding acquisition. **V.G. Kouznetsova:** Conceptualization, Writing – review & editing, Supervision, Funding acquisition.

Declaration of competing interest

The authors declare that they have no known competing financial interests or personal relationships that could have appeared to influence the work reported in this paper.

Data availability

Data will be made available on request.

Acknowledgements

This research was carried out under project number T17019d in the framework of the research program of the Materials Innovation Institute (M2i) (www.m2i.nl) supported by the Dutch government. The authors gratefully acknowledge Tijmen Vermeij and Roy L.A. Kerkhof for providing SEM micrographs in Fig. 1.

Appendix A. Microscopic unit cell boundary conditions

This appendix details the microscopic M/F interfacial zone unit cell boundary conditions introduced in Section 3. These boundary conditions customized for the microscale model are formulated to avoid spurious excessive deformation at non-periodic parts of the boundary containing a soft phase.

The unit cell boundary conditions are derived following the standard kinematics scale transition used in classical computational homogenization frameworks (see e.g. Geers et al., 2017). To this aim, the relative position vector field $\Delta\vec{x}_{\mathrm{m}}$ in the current, deformed configuration within the microscopic unit cell $\mathcal{V}_{\mathrm{m}}$ (see Fig. A.16) is expressed in terms of the mesoscopic deformation gradient $\boldsymbol{\mathcal{F}}_{\mathrm{IZ}}$ as

$$\Delta\vec{x}_{\mathrm{m}} = \boldsymbol{\mathcal{F}}_{\mathrm{IZ}} \cdot \Delta\vec{X}_{\mathrm{m}} + \Delta\vec{w}_{\mathrm{m}} \quad \text{in } \mathcal{V}_{\mathrm{m}}, \tag{A.1}$$

where $\Delta\vec{X}_{\mathrm{m}} = \vec{X}_{\mathrm{m}} - \vec{X}_{\mathrm{m,c}}$, $\Delta\vec{x}_{\mathrm{m}} = \vec{x}_{\mathrm{m}} - \vec{x}_{\mathrm{m,c}}$ and $\Delta\vec{w}_{\mathrm{m}} = \vec{w}_{\mathrm{m}} - \vec{w}_{\mathrm{m,c}}$ with subscript "c" denoting a (arbitrary) reference point; $\vec{X}_{\mathrm{m}}$ indicates the position vector of a point in the initial, undeformed configuration and $\vec{w}_{\mathrm{m}}$ is the microfluctuation field induced by the microstructural heterogeneities.

Substituting Eq. (A.1) into the definition of the microscopic deformation gradient $\mathbf{F}_{\mathrm{m}} = (\vec{\nabla}_{0\mathrm{m}}\vec{x}_{\mathrm{m}})^{\mathrm{T}} = \boldsymbol{\mathcal{F}}_{\mathrm{IZ}} + (\vec{\nabla}_{0\mathrm{m}}\Delta\vec{w}_{\mathrm{m}})^{\mathrm{T}}$ and requiring the scale transition relation between the micro- and mesoscale deformation gradient tensors to hold

$$\boldsymbol{\mathcal{F}}_{\mathrm{IZ}} = \frac{1}{V_{\mathrm{m}}} \int_{\mathcal{V}_{\mathrm{m}}} \mathbf{F}_{\mathrm{m}} \, \mathrm{d}V_{\mathrm{m}}, \tag{A.2}$$

yields, upon using the Gauss's theorem, the boundary conditions for the microfluctuation field

$$\int_{\mathcal{S}_{\mathrm{m}}} \Delta\vec{w}_{\mathrm{m}} \otimes \vec{N}_{\mathrm{m}} \, \mathrm{d}S_{\mathrm{m}} = \mathbf{0}, \tag{A.3}$$

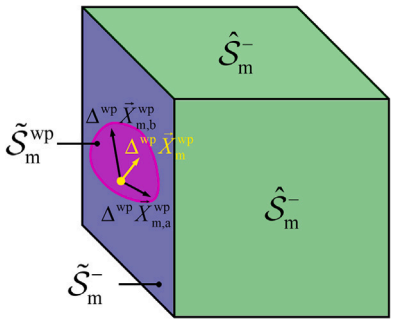

Fig. A.16. 3D sketch of the unit cell with the boundary parts $\hat{\mathcal{S}}_{\mathrm{m}}^{-}$, $\tilde{\mathcal{S}}_{\mathrm{m}}^{-}$, and $\tilde{\mathcal{S}}_{\mathrm{m}}^{\mathrm{wp}}$ containing the soft phase, indicated by the green, blue and pink shadows, respectively. The boundaries $\hat{\mathcal{S}}_{\mathrm{m}}^{+}$ and $\tilde{\mathcal{S}}_{\mathrm{m}}^{+}$ opposite to $\hat{\mathcal{S}}_{\mathrm{m}}^{-}$ and $\tilde{\mathcal{S}}_{\mathrm{m}}^{-}$, respectively, are not visible.

where $\vec{N}_{\mathrm{m}}$ denotes the outward normal of the unit cell boundary $\mathcal{S}_{\mathrm{m}}$.

In classical homogenization frameworks, periodic boundary conditions (Geers et al., 2017) are often adopted to satisfy condition (A.3). For the microscopic M/F interfacial zone unit cell (see Fig. 3), periodic boundary conditions remain suitable for the transverse boundary pair $\hat{\mathcal{S}}_{\mathrm{m}}^{-/+}$. Taking into account that $\vec{N}_{\mathrm{m}}^{-} = -\vec{N}_{\mathrm{m}}^{+}$, the periodicity conditions for the transverse boundaries then read:

$$\Delta\vec{w}_{\mathrm{m}}^{-} - \Delta\vec{w}_{\mathrm{m}}^{+} = \vec{0} \quad \text{on } \hat{\mathcal{S}}_{\mathrm{m}}. \tag{A.4}$$

For the remaining boundary pair $\tilde{\mathcal{S}}_{\mathrm{m}}^{-/+}$, however, the periodicity conditions may not be prescribed, since $\tilde{\mathcal{S}}_{\mathrm{m}}^{-}$ and $\tilde{\mathcal{S}}_{\mathrm{m}}^{+}$ are morphologically not periodic and contain three different phases with highly contrasting and anisotropic properties, i.e. ferrite (F), martensite laths (ML), and retained austenite (RA). Therefore, again taking into account that the normal vectors on the opposite unit cell boundaries have opposite directions, the condition (A.3) on $\tilde{\mathcal{S}}_{\mathrm{m}}^{-/+}$ remains in the form of the minimal kinematic boundary conditions (Miehe, 2002; Mesarovic and Padbidri, 2005):

$$\int_{\tilde{\mathcal{S}}_{\mathrm{m}}} (\Delta\vec{w}_{\mathrm{m}}^{-} - \Delta\vec{w}_{\mathrm{m}}^{+})\,\mathrm{d}S_{\mathrm{m}} = \vec{0}. \tag{A.5}$$

It is, however, known (Miehe, 2002; Coenen et al., 2012) that for microstructures with highly contrasting properties of its constituents, the minimal kinematic boundary conditions can lead to spurious excessive deformation of the soft phase near the unit cell boundaries. To prevent this, an additional constraint is imposed. Assuming that all points on the soft phase part of the boundary $\tilde{\mathcal{S}}_{\mathrm{m}}^{\mathrm{wp}}$ lie in one plane in the reference configuration, it is required that these points remain in one plane during the deformation. This constraint can be satisfied by selecting two non-collinear arbitrary vectors $\Delta\vec{x}_{\mathrm{m,a}}^{\mathrm{wp}}(\Delta\vec{X}_{\mathrm{m,a}}^{\mathrm{wp}})$ and $\Delta\vec{x}_{\mathrm{m,b}}^{\mathrm{wp}}(\Delta\vec{X}_{\mathrm{m,b}}^{\mathrm{wp}})$ and enforcing the following constraint for all points of the soft phase of the boundary:

$$\Delta^{\mathrm{wp}}\vec{x}_{\mathrm{m}}^{\mathrm{wp}} = c_{\mathrm{a}}\Delta^{\mathrm{wp}}\vec{x}_{\mathrm{m,a}}^{\mathrm{wp}} + c_{\mathrm{b}}\Delta^{\mathrm{wp}}\vec{x}_{\mathrm{m,b}}^{\mathrm{wp}} \quad \forall\vec{X}_{\mathrm{m}}^{\mathrm{wp}} \in \tilde{\mathcal{S}}_{\mathrm{m}}^{\mathrm{wp}}, \tag{A.6}$$

where Δ^{wp} is taken with respect to an arbitrary point (see the yellow point in Fig. A.16) on $\tilde{\mathcal{S}}_{\mathrm{m}}^{\mathrm{wp}}$, and c_{a} and c_{b} are two coefficients determined from $\Delta^{\mathrm{wp}}\vec{X}_{\mathrm{m}}^{\mathrm{wp}} = c_{\mathrm{a}}\Delta^{\mathrm{wp}}\vec{X}_{\mathrm{m,a}}^{\mathrm{wp}} + c_{\mathrm{b}}\Delta^{\mathrm{wp}}\vec{X}_{\mathrm{m,b}}^{\mathrm{wp}}$, implying a linear transformation constraint on $\tilde{\mathcal{S}}_{\mathrm{m}}^{\mathrm{wp}}$. Notice that with this additional constraint (A.6), only the boundary part $\tilde{\mathcal{S}}_{\mathrm{m}}^{\mathrm{wp}}$ remains planar during the deformation while not for the boundary part $\tilde{\mathcal{S}}_{\mathrm{m}}^{-}/\tilde{\mathcal{S}}_{\mathrm{m}}^{\mathrm{wp}}$ (see the blue area surrounding the pink area in Fig. A.16).

The combination of the above constraints (A.4)–(A.6) forms the boundary conditions for the microscopic unit cell simulations in this study.

Finally, note that for the convenience of numerical implementation, the conditions (A.4) and (A.5) can be expressed in terms of the current configuration position vectors of the points as

$$\Delta\vec{x}_{\mathrm{m}}^{-} - \Delta\vec{x}_{\mathrm{m}}^{+} = \boldsymbol{\mathcal{F}}_{\mathrm{IZ}} \cdot (\Delta\vec{X}_{\mathrm{m}}^{-} - \Delta\vec{X}_{\mathrm{m}}^{+}) \quad \text{on } \hat{\mathcal{S}}_{\mathrm{m}}, \tag{A.7a}$$

$$\int_{\tilde{\mathcal{S}}_{\mathrm{m}}} (\Delta\vec{x}_{\mathrm{m}}^{-} - \Delta\vec{x}_{\mathrm{m}}^{+})\,\mathrm{d}S_{\mathrm{m}} = \boldsymbol{\mathcal{F}}_{\mathrm{IZ}} \cdot \int_{\tilde{\mathcal{S}}_{\mathrm{m}}} (\Delta\vec{X}_{\mathrm{m}}^{-} - \Delta\vec{X}_{\mathrm{m}}^{+})\,\mathrm{d}S_{\mathrm{m}}. \tag{A.7b}$$

Appendix B. Material models at the microscale

The material models of the martensite island (martensite/austenite laminate, M/A) and the ferrite matrix adopted for the microscopic M/F interfacial zone unit cell simulations defined in Section 3 are detailed in this appendix.

B.1. Lath and retained austenite film

A conventional finite deformation crystal plasticity model (see e.g. Kalidindi et al., 1992) is employed to describe both BCC laths and FCC retained austenite (RA) films. The total defamation gradient $\mathbf{F}$ is decomposed into the elastic ($\mathbf{F}_e$) and plastic ($\mathbf{F}_p$) parts as $\mathbf{F} = \mathbf{F}_e \cdot \mathbf{F}_p$. The elastic regime is described by the linear relation $\bar{\mathbf{S}} = \mathbb{C} : \bar{\mathbf{E}}_e$, where $\bar{\mathbf{S}} = \mathbf{F}_p \cdot \mathbf{S} \cdot \mathbf{F}_p^T$ denotes the push-forward of the second Piola–Kirchhoff stress tensor $\mathbf{S}$ towards the intermediate configuration and $\bar{\mathbf{E}}_e = \frac{1}{2}(\bar{\mathbf{C}}_e - \mathbf{I})$ is the elastic Green–Lagrange strain tensor with $\bar{\mathbf{C}}_e = \mathbf{F}_e^T \cdot \mathbf{F}_e$. The cubic elasticity tensor $\mathbb{C}$ is fully determined by specifying the three elastic constants C_{11}, C_{12} and C_{44}. The plastic velocity gradient tensor $\mathbf{L}_p = \dot{\mathbf{F}}_p \cdot \mathbf{F}_p^{-1}$ is computed as a function of the slip rate $\dot{\gamma}^\alpha$ and the Schmid tensor $\mathbf{P}_0^\alpha$ of each of the N_s slip systems as $\mathbf{L}_p = \sum_{\alpha=1}^{N_s} \dot{\gamma}^\alpha \mathbf{P}_0^\alpha$. The crystallographic slip $\dot{\gamma}^\alpha$ of the α-th slip system is driven by the resolved shear stress $\tau^\alpha = \bar{\mathbf{S}} \cdot \bar{\mathbf{C}}_e : \mathbf{P}_0^\alpha$ and computed by means of a power law (Hutchinson, 1976)

$$\dot{\gamma}^\alpha = \dot{\gamma}_0^\alpha \left(\frac{|\tau^\alpha|}{s^\alpha} \right)^{\frac{1}{m}} \operatorname{sign}(\tau^\alpha), \tag{B.1}$$

where $\dot{\gamma}_0^\alpha$ denotes the reference slip rate, s^α the slip resistance and m the slip rate sensitivity. Hardening is included through the evolution of the slip resistance s^α given by Wu et al. (1991)

$$\dot{s}^\alpha = \sum_{\beta=1}^{N_s} h^{\alpha\beta} |\dot{\gamma}^\beta|, \tag{B.2}$$

with the initial slip resistance $s^\alpha(0) = s_0$ and the hardening moduli $h^{\alpha\beta}$ defined as

$$h^{\alpha\beta} = h_0 \left(1 - \frac{s^\alpha}{s_\infty} \right)^n [q + (1-q)\delta^{\alpha\beta}], \tag{B.3}$$

where h_0 denotes the reference hardening modulus, s_∞ the saturation slip resistance, n the hardening exponent, q the latent/self hardening modulus ratio; δ is the Kronecker delta.

B.2. Ferrite matrix

A finite strain isotropic elasto-plasticity is used to describe the behaviour of the ferrite matrix. The elastic regime follows the linear relation $\bar{\mathbf{S}} = \mathbb{C} : \bar{\mathbf{E}}_e$. The isotropic elasticity tensor $\mathbb{C}$ is determined by Young's modulus E and Poisson's ratio ν. In the plastic regime, the von Mises yield condition is employed, in terms of the equivalent von Mises stress $S^{eq} = \sqrt{\frac{3}{2}\bar{\mathbf{S}}_{dev} : \bar{\mathbf{S}}_{dev}}$, where $(\bullet)_{dev}$ denotes the deviatoric part of a second-order tensor, and the equivalent plastic strain rate $\dot{E}_p^{eq} = \sqrt{\frac{2}{3}\dot{\mathbf{E}}_p : \dot{\mathbf{E}}_p}$. An exponentially saturating hardening law is selected to account for the evolution of yield stress S_y up to a saturation yield stress S_∞ (Brown et al., 1989), reading

$$S_y = S_\infty - (S_\infty - S_0) \exp\left(-\frac{E_p^{eq}}{E_c} \right), \tag{B.4}$$

where S_0 denotes the initial yield stress, E_c the characteristic strain and $E_p^{eq} = \int \dot{E}_p^{eq}\, dt$ the (accumulated) equivalent plastic strain.

Appendix C. Material model for the martensite islands at the mesoscale

In this appendix, the reduced model (Maresca et al., 2016b) for the martensite islands used at the DP steel mesoscopic simulations defined in Section 7 is briefly summarized.

C.1. Lamella model

A martensite substructure (more generally, (sub-)blocks) can be approximated by an infinite stack of martensite laths with RA films in between, see Fig. C.17, which can be described by a multi-scale lamella model (Maresca et al., 2014b). The equations of the lamella model are given by Maresca et al. (2014b):

$$\mathbf{F}_{M/A} = (1 - f_{RA})\mathbf{F}_{ML} + f_{RA}\mathbf{F}_{RA}, \tag{C.1a}$$

$$\mathbf{P}_{M/A} = (1 - f_{RA})\mathbf{P}_{ML} + f_{RA}\mathbf{P}_{RA}, \tag{C.1b}$$

$$\mathbf{P}_{ML} \cdot \vec{N}^{hp} = \mathbf{P}_{RA} \cdot \vec{N}^{hp}, \tag{C.1c}$$

$$\mathbf{F}_{ML} \cdot (\mathbf{I} - \vec{N}^{hp} \otimes \vec{N}^{hp}) = \mathbf{F}_{RA} \cdot (\mathbf{I} - \vec{N}^{hp} \otimes \vec{N}^{hp}), \tag{C.1d}$$

where $\mathbf{F}_{M/A}$ and $\mathbf{P}_{M/A}$ denote the effective deformation gradient tensor and first Piola–Kirchhoff stress tensor of the martensite substructure, obtained through homogenization, by volume averaging the individual phase quantities; f_{RA} is the RA volume fraction within the martensite substructure; Eqs. (C.1c) and (C.1d) are the traction equilibrium and deformation compatibility to be satisfied at the M/RA interface, the normal coincides with the habit plane normal. In the considered mesoscopic simulations, each martensite

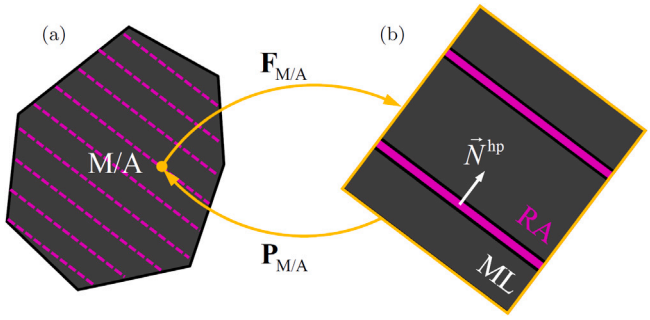

Fig. C.17. A multi-scale lamella model for the martensite island: (a) mesoscopic configuration and (b) underlying microstructure consisting of a stack of martensite laths and RA films. The laths and RA films are not spatially resolved at the mesoscale, but only accounted for through the effective behaviour.

island is assumed to consist of laths belonging to the same variant. Therefore, the above lamella model has been directly adopted to describe the martensite island behaviour.

The constitutive models (Maresca et al., 2016b) for the FCC RA films and the BCC laths needed to complete the lamella model (C.1) are detailed next.

C.2. Reduced crystal plasticity models for lath and retained austenite film

In the elastic regime, both martensite laths and RA films within the lamella model follow a linear relation $\bar{\mathbf{S}} = \mathbb{C} : \bar{\mathbf{E}}_{\mathrm{e}}$.

For the RA films in the plastic regime, the plastic velocity gradient tensor consists of two contributions, i.e. $\mathbf{L}_{\mathrm{p}} = \mathbf{L}_{\mathrm{p},\gamma} + \mathbf{L}_{\mathrm{p},\varepsilon}$. The slip contribution $\mathbf{L}_{\mathrm{p},\gamma} = \sum_{\alpha=1}^{3} \dot{\gamma}^{\alpha} \mathbf{P}_0^{\alpha}$ accounts for the plastic slip on the three specific FCC slip systems parallel to the habit plane. The crystallographic slip on each of these slip systems is computed following the standard crystal plasticity formulation (see Appendix B). The isotropic contribution $\mathbf{L}_{\mathrm{p},\varepsilon}$ accounts for the plastic deformation in other directions of the RA films and is computed as $\mathbf{L}_{\mathrm{p},\varepsilon} = \dot{\varepsilon}_{\mathrm{p}}^{\mathrm{eq}} \mathbf{N}_{\varepsilon}$, where $\dot{\varepsilon}_{\mathrm{p}}^{\mathrm{eq}}$ denotes the equivalent plastic strain rate, $\mathbf{N}_{\varepsilon} = \frac{3\bar{\mathbf{M}}_{\mathrm{dev}}}{2M^{\mathrm{eq}}}$ is the flow direction, $\bar{\mathbf{M}} = \bar{\mathbf{S}} \cdot \bar{\mathbf{C}}_{\mathrm{e}} : \mathbb{P}_{\varepsilon}$ the Mandel stress tensor projected using the fourth-order tensor $\mathbb{P}_{\varepsilon}$ onto the space orthogonal to the space spanned by $\mathbf{P}_0^{\alpha}$, and M^{eq} is the equivalent von Mises stress. The equivalent plastic strain rate related to the isotropic contribution, $\dot{\varepsilon}_{\mathrm{p}}^{\mathrm{eq}}$, is driven by the equivalent stress M^{eq} and computed using the rate-dependent power law

$$\dot{\varepsilon}_{\mathrm{p}}^{\mathrm{eq}} = \dot{\varepsilon}_0 \left(\frac{M^{\mathrm{eq}}}{M_{\mathrm{y}}} \right)^{\frac{1}{a}}, \tag{C.2}$$

where $\dot{\varepsilon}_0$ denotes the reference strain rate, M_{y} the yield stress and a the strain rate sensitivity. The evolution law for the yield stress M_{y} is taken as

$$\dot{M}_{\mathrm{y}} = H \dot{\varepsilon}_{\mathrm{p}}^{\mathrm{eq}}, \tag{C.3}$$

with the initial yield stress $M_{\mathrm{y}}(0) = M_0$ and the hardening modulus

$$H = H_0 \left(1 - \frac{M_{\mathrm{y}}}{M_{\infty}} \right)^{b}, \tag{C.4}$$

where H_0 denotes the reference hardening modulus, M_{∞} the saturation yield stress and b the hardening exponent.

As observed from the microscopic M/F interfacial zone unit cell simulations, the plastic slip within the martensite laths is limited,in case of highly active sliding, which is of interest here. Thus, the plastic deformation of the laths in the lamella model is described using isotropic (visco-)plasticity as described above, but with $\mathbb{P}_{\varepsilon} = \mathbb{I}$, i.e. in this case no discrete slip directions are taken into account and the equivalent plastic strain rate in entirely determined using Eqs. (C.2)–(C.4).

C.3. Parameter identification of the isotropic contribution in the reduced martensite island model

The parameter identification of the reduced model (Maresca et al., 2016b) adopted for the martensite islands at the mesoscale is detailed in the following.

The anisotropic elastic behaviour of the FCC RA films and BCC laths is described using the same elastic constants as those given in Table 1. For the RA films, the parameters for the plastic slip on the three distinct slip systems in the habit plane are the same as those listed in Table 1, for the full crystal plasticity modelling.

The isotropic plasticity parameters of the RA films and martensite laths are linked to the respective crystal plasticity model parameters through the Taylor factor $\mathcal{T}$, i.e. the isotropic initial yield stress M_0, the saturation yield stress M_{∞} and the reference hardening modulus H_0 are obtained as

$$M_0 = \mathcal{T} s_0, \tag{C.5a}$$

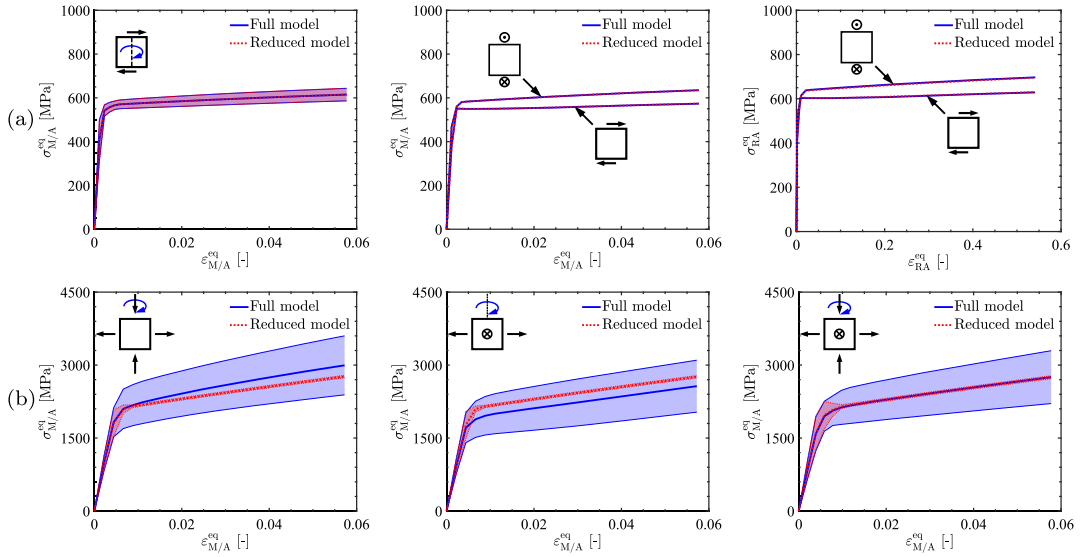

Fig. C.18. Comparison between the effective stresses versus effective applied strains obtained using the fully resolved crystal plasticity and reduced modelling of an infinite laminate consisting of the martensite laths and RA films under different overall loading types: (a) simple shear in different directions parallel to the habit plane, and (b) biaxial and triaxial deformations in different directions.

$$M_\infty = \mathcal{T} s_\infty, \tag{C.5b}$$

$$H_0 = (1 + (\mathcal{T} - 1)q)\,\mathcal{T} h_0, \tag{C.5c}$$

where for the isotropic reference hardening modulus H_0, the latent hardening effect has been taken into account by introducing an extra factor $1 + (\mathcal{T} - 1)q$, which involves the latent/self hardening ratio q. A Taylor factor $\mathcal{T} = 3.07$ is adopted for the FCC RA films, which is a typical value used in the literature for crystals with one active slip family (Rosenberg and Piehler, 1971). Since for the BCC laths, two slip families are considered in this study, a somewhat lower Taylor factor $\mathcal{T} = 2.95$ is used (Rosenberg and Piehler, 1971). Substituting the above Taylor factor values and the latent/self hardening ratio $q = 1.4$ from Table 1 into Eq. (C.5) leads to the isotropic parameters for the RA films and laths. For consistency with the crystal plasticity modelling, the reference strain rate, strain rate sensitivity and hardening exponent are taken as $\dot{\varepsilon}_0 = \dot{\gamma}_0$, $a = m$ and $b = n$, respectively. The resulting material parameters for the isotropic contributions are listed in Table 3.

Extensive numerical simulations are performed to validate the reduced lath martensite model with the identified parameters against the fully resolved crystal plasticity model. An infinite laminate consisting of the martensite laths and RA films is considered, with the crystallographic orientations of both phases the same as shown in Fig. 4. Four different overall deformation gradient tensors are applied on the laminate, defined with respect to the coordinate axis directions indicated in Fig. 4:

- in-plane simple shear $\langle \mathbf{F} \rangle_0 = \mathbf{I} + \gamma \vec{e}_x \vec{e}_y$,
- in-plane biaxial loading $\langle \mathbf{F} \rangle_0 = \lambda \vec{e}_x \otimes \vec{e}_x + \frac{1}{\lambda} \vec{e}_y \otimes \vec{e}_y + \vec{e}_z \otimes \vec{e}_z$,
- out-of-plane biaxial loading $\langle \mathbf{F} \rangle_0 = \lambda \vec{e}_x \otimes \vec{e}_x + \vec{e}_y \otimes \vec{e}_y + \frac{1}{\lambda} \vec{e}_z \otimes \vec{e}_z$,
- triaxial loading $\langle \mathbf{F} \rangle_0 = \lambda \vec{e}_x \otimes \vec{e}_x + \frac{1}{\sqrt{\lambda}} \vec{e}_y \otimes \vec{e}_y + \frac{1}{\sqrt{\lambda}} \vec{e}_z \otimes \vec{e}_z$.

Here, γ denotes the applied shear magnitude and λ the applied stretch ratio. To study the influence of different loading directions, the prescribed overall deformations have been rotated around the habit plane normal (i.e. Y axis in Fig. 4).

The results are shown in Fig. C.18. For each loading type, the direction-averaged effective response is reported, together with its standard deviation. The simple shear deformation parallel to the habit plane activates the substructure boundary sliding, which is predominantly realized by plastic slip on the three FCC slip systems parallel to the habit plane. As expected, this case is exceptionally well captured by the reduced model, as can be seen in Fig. C.18(a). The dependency on the simple shear direction is small and can be traced back to the minor anisotropy of the RA film in the habit plane, see the middle and right in Fig. C.18(a).

Under biaxial and triaxial deformations, where the sliding is inactive, the reduced model is still able to reproduce the direction-averaged effective responses reasonably well, as shown in Fig. C.18(b). In particular, under triaxial deformation, the difference between the direction-averaged effective responses obtained using two models, are almost invisible. This may be attributed to the fact that more slip systems are activated under the triaxial deformation compared to the biaxial deformation, leading to a better approximation of the crystal response through the Taylor factor. The pronounced direction dependency of the effective responses in the cases of inactive sliding is also clearly observed in Fig. C.18(b), which is due to the lath anisotropy. This direction dependency is not captured by the reduced model, where an isotropic plastic behaviour of the laths is assumed.

Based on the above numerical examinations and the early stated hypothesis that the sliding-induced deformation mode is favourable to occur for the martensite islands, it is concluded that the reduced martensite island model is able to approximate the fully resolved model with adequate accuracy.

References

Abid, N.H., Abu Al-Rub, R.K., Palazotto, A.N., 2017. Micromechanical finite element analysis of the effects of martensite particle size and ferrite grain boundaries on the overall mechanical behavior of dual phase steel. J. Eng. Mater. Technol. 139 (4), 041006.

Ahmadi, M., Hosseini-Toudeshky, H., Sadighi, M., 2020. Peridynamic micromechanical modeling of plastic deformation and progressive damage prediction in dual-phase materials. Eng. Fract. Mech. 235, 107179.

Brown, S., Kim, K., Anand, L., 1989. An internal variable constitutive model for hot working of metals. Int. J. Plast. 5 (2), 95–130.

Calcagnotto, M., Ponge, D., Raabe, D., 2010. Effect of grain refinement to 1μm on strength and toughness of dual-phase steels. Mater. Sci. Eng. A 527 (29–30), 7832–7840.

Chehab, B., Wang, X., Masse, J-P., Bouaziz, O., Zurob, H., Embury, D., 2010. Bulk nanoscale materials in steel products. J. Phys. Conf. Ser. 240, 012135.

Coenen, E.W.C., Kouznetsova, V.G., Geers, M.G.D., 2012. Novel boundary conditions for strain localization analyses in microstructural volume elements. Internat. J. Numer. Methods Engrg. 90 (1), 1–21.

de Geus, T.W.J., Maresca, F., Peerlings, R.H.J., Geers, M.G.D., 2016. Microscopic plasticity and damage in two-phase steels: On the competing role of crystallography and phase contrast. Mech. Mater. 101, 147–159.

Du, C., Hoefnagels, J.P.M., Vaes, R., Geers, M.G.D., 2016. Plasticity of lath martensite by sliding of substructure boundaries. Scr. Mater. 120, 37–40.

Du, C., Petrov, R., Geers, M.G.D., Hoefnagels, J.P.M., 2019. Lath martensite plasticity enabled by apparent sliding of substructure boundaries. Mater. Des. 172, 107646.

Furukimi, O., Kiattisaksri, C., Takeda, Y., Aramaki, M., Oue, S., Munetoh, S., Tanaka, M., 2017. Void nucleation behavior of single-crystal high-purity iron specimens subjected to tensile deformation. Mater. Sci. Eng. A 701, 221–225.

Geers, M.G.D., Kouznetsova, V.G., Matouš, K., Yvonnet, J., 2017. Homogenization methods and multiscale modeling: Nonlinear problems. In: Encyclopedia of Computational Mechanics Second Edition. John Wiley & Sons, Ltd, Chichester, pp. 1–34.

Ghadbeigi, H., Pinna, C., Celotto, S., 2013. Failure mechanisms in DP600 steel: Initiation, evolution and fracture. Mater. Sci. Eng. A 588, 420–431.

Ghadbeigi, H., Pinna, C., Celotto, S., Yates, J.R., 2010. Local plastic strain evolution in a high strength dual-phase steel. Mater. Sci. Eng. A 527 (18–19), 5026–5032.

Ghaffarian, H., Na, Y., Jang, D., 2022. Interfacial plasticity mediated by lath boundaries in reduced-activation ferritic/martensitic steels. J. Nucl. Mater. 559, 153439.

Hoefnagels, J.P.M., Tasan, C.C., Maresca, F., Peters, F.J., Kouznetsova, V.G., 2015. Retardation of plastic instability via damage-enabled microstrain delocalization. J. Mater. Sci. 50 (21), 6882–6897.

Hosseini-Toudeshky, H., Anbarlooie, B., Kadkhodapour, J., 2015. Micromechanics stress–strain behavior prediction of dual phase steel considering plasticity and grain boundaries debonding. Mater. Des. 68, 167–176.

Hutchinson, J.W., 1976. Bounds and self-consistent estimates for creep of polycrystalline materials. Proc. R. Soc. A Math. Phys. Eng. Sci. 348 (1652), 101–127.

Inoue, J., Sadeghi, A., Koseki, T., 2019. Slip band formation at free surface of lath martensite in low carbon steel. Acta Mater. 165, 129–141.

Isik, K., Gerstein, G., Clausmeyer, T., Nürnberger, F., Tekkaya, A.E., Maier, H.J., 2016. Evaluation of void nucleation and development during plastic deformation of dual-phase steel DP600. Steel Res. Int. 87 (12), 1583–1591.

Johnson, G.R., Cook, W.H., 1985. Fracture characteristics of three metals subjected to various strains, strain rates, temperatures and pressures. Eng. Fract. Mech. 21 (1), 31–48.

Kadkhodapour, J., Schmauder, S., Raabe, D., Ziaei-Rad, S., Weber, U., Calcagnotto, M., 2011. Experimental and numerical study on geometrically necessary dislocations and non-homogeneous mechanical properties of the ferrite phase in dual phase steels. Acta Mater. 59 (11), 4387–4394.

Kalidindi, S.R., Bronkhorst, C.A., Anand, L., 1992. Crystallographic texture evolution in bulk deformation processing of FCC metals. J. Mech. Phys. Solids 40 (3), 537–569.

Kamikawa, N., Hirohashi, M., Sato, Y., Chandiran, E., Miyamoto, G., Furuhara, T., 2015. Tensile behavior of ferrite-martensite dual phase steels with nano-precipitation of vanadium carbides. ISIJ Int. 55 (8), 1781–1790.

Kang, J., Ososkov, Y., Embury, J.D., Wilkinson, D.S., 2007. Digital image correlation studies for microscopic strain distribution and damage in dual phase steels. Scr. Mater. 56 (11), 999–1002.

Kelly, P.M., Jostsons, A., Blake, R.G., 1990. The orientation relationship between lath martensite and austenite in low carbon, low alloy steels. Acta Metall. Mater. 38 (6), 1075–1081.

Kim, D.K., Kim, E.Y., Han, J., Woo, W., Choi, S.H., 2017. Effect of microstructural factors on void formation by ferrite/martensite interface decohesion in DP980 steel under uniaxial tension. Int. J. Plast. 94, 3–23.

Krauss, G., Marder, A.R., 1971. The morphology of martensite in iron alloys. Metall. Trans. 2 (9), 2343–2357.

Liao, X., Wang, X., Guo, Z., Wang, M., Wu, Y., Rong, Y., 2010. Microstructures in a resistance spot welded high strength dual phase steel. Mater. Charact. 61 (3), 341–346.

Liu, L., Maresca, F., Hoefnagels, J.P.M., Vermeij, T., Geers, M.G.D., Kouznetsova, V.G., 2021. Revisiting the martensite/ferrite interface damage initiation mechanism: The key role of substructure boundary sliding. Acta Mater. 205, 116533.

Lutsey, N., 2010. Review of Technical Literature and Trends Related to Automobile Mass-Reduction Technology. Technical report, University of California, Davis.

Maire, E., Bouaziz, O., Di Michiel, M., Verdu, C., 2008. Initiation and growth of damage in a dual-phase steel observed by X-ray microtomography. Acta Mater. 56 (18), 4954–4964.

Maresca, F., Kouznetsova, V.G., Geers, M.G.D., 2014a. On the role of interlath retained austenite in the deformation of lath martensite. Modelling Simulation Mater. Sci. Eng. 22 (4), 045011.

Maresca, F., Kouznetsova, V.G., Geers, M.G.D., 2014b. Subgrain lath martensite mechanics: A numerical–experimental analysis. J. Mech. Phys. Solids 73, 69–83.

Maresca, F., Kouznetsova, V.G., Geers, M.G.D., 2016a. Deformation behaviour of lath martensite in multi-phase steels. Scr. Mater. 110, 74–77.

Maresca, F., Kouznetsova, V.G., Geers, M.G.D., 2016b. Reduced crystal plasticity for materials with constrained slip activity. Mech. Mater. 92, 198–210.

Maresca, F., Kouznetsova, V.G., Geers, M.G.D., Curtin, W.A., 2018. Contribution of austenite-martensite transformation to deformability of advanced high strength steels: From atomistic mechanisms to microstructural response. Acta Mater. 156, 463–478.

Mazinani, M., Poole, W.J., 2007. Effect of martensite plasticity on the deformation behavior of a low-carbon dual-phase steel. Metall. Mater. Trans. A 38 (2), 328–339.

Mesarovic, S.D., Padbidri, J., 2005. Minimal kinematic boundary conditions for simulations of disordered microstructures. Phil. Mag. 85 (1), 65–78.

Miehe, C., 2002. Strain-driven homogenization of inelastic microstructures and composites based on an incremental variational formulation. Internat. J. Numer. Methods Engrg. 55 (11), 1285–1322.

Morito, S., Huang, X., Furuhara, T., Maki, T., Hansen, N., 2006. The morphology and crystallography of lath martensite in alloy steels. Acta Mater. 54 (19), 5323–5331.

Morito, S., Oh-ishi, K., Hono, K., Ohba, T., 2011. Carbon enrichment in retained austenite films in low carbon lath martensite steel. ISIJ Int. 51 (7), 1200–1202.
Morito, S., Tanaka, H., Konishi, R., Furuhara, T., Maki, T., 2003. The morphology and crystallography of lath martensite in Fe-C alloys. Acta Mater. 51 (6), 1789–1799.
Morsdorf, L., Jeannin, O., D., Barbier, M., Mitsuhara, Raabe, D., Tasan, C.C., 2016. Multiple mechanisms of lath martensite plasticity. Acta Mater. 121, 202–214.
Ohmura, T., Minor, A.M., Stach, E.A., Morris, J.W., 2004. Dislocation–grain boundary interactions in martensitic steel observed through in situ nanoindentation in a transmission electron microscope. J. Mater. Res. 19 (12), 3626–3632.
Pierman, A.P., Bouaziz, O., Pardoen, T., Jacques, P.J., Brassart, L., 2014. The influence of microstructure and composition on the plastic behaviour of dual-phase steels. Acta Mater. 73, 298–311.
Raabe, D., Zhao, Z., Roters, F., 2001. A finite element method on the basis of texture components for fast predictions of anisotropic forming operations. Steel Res. 72 (10), 421–426.
Rice, J.R., Tracey, D.M., 1969. On the ductile enlargement of voids in triaxial stress fields. J. Mech. Phys. Solids 17 (3), 201–217.
Rosenberg, J.M., Piehler, H.R., 1971. Calculation of the taylor factor and lattice rotations for bcc metals deforming by pencil glide. Metall. Trans. 2 (1), 257–259.
Sandvik, B.P.J., Wayman, C.M., 1983. Crystallography and substructure of lath martensite formed in carbon steels. Metallography 16 (2), 199–227.
Sodjit, S., Uthaisangsuk, V., 2012. Microstructure based prediction of strain hardening behavior of dual phase steels. Mater. Des. 41, 370–379.
Sun, S., Pugh, M., 2002. Properties of thermomechanically processed dual-phase steels containing fibrous martensite. Mater. Sci. Eng. A 335 (1–2), 298–308.
Tang, A., Liu, H., Chen, R., Liu, G., Lai, Q., Zhong, Y., Wang, L., Wang, J., Lu, Q., Shen, Y., 2021. Mesoscopic origin of damage nucleation in dual-phase steels. Int. J. Plast. 137, 102920.
Tasan, C.C., Hoefnagels, J.P.M., Diehl, M., Yan, D., Roters, F., Raabe, D., 2014. Strain localization and damage in dual phase steels investigated by coupled in-situ deformation experiments and crystal plasticity simulations. Int. J. Plast. 63, 198–210.
Tian, C., Ponge, D., Christiansen, L., Kirchlechner, C., 2020. On the mechanical heterogeneity in dual phase steel grades: Activation of slip systems and deformation of martensite in DP800. Acta Mater. 183, 274–284.
Uthaisangsuk, V., Prahl, U., Bleck, W., 2011. Modelling of damage and failure in multiphase high strength DP and TRIP steels. Eng. Fract. Mech. 78 (3), 469–486.
Vermeij, T., Kerkhof, R.L.A., Hoefnagels, J.P.M., 2022a. Favorable lath martensite plasticity mechanisms in dual-phase steel: substructure boundary sliding and habit plane slip. (in preparation).
Vermeij, T., Verstijnen, J.A.C., Ramirez y Cantador, T., Blaysat, B., Neggers, J., Hoefnagels, J.P.M., 2022b. A nanomechanical testing framework yielding front & rear-sided, high-resolution, microstructure-correlated SEM-DIC strain fields. Exp. Mech. (in press).
Wan, V.V.C., MacLachlan, D.W., Dunne, F.P.E., 2014. A stored energy criterion for fatigue crack nucleation in polycrystals. Int. J. Fatigue 68, 90–102.
Wu, T.Y., Bassani, J.L., Laird, C., 1991. Latent hardening in single crystals I: theory and experiments. Proc. R. Soc. A Math. Phys. Eng. Sci. 435 (1893), 1–19.
Yoshida, H., Takagi, S., Sakai, S., Morito, S., Ohba, T., 2015. Crystallographic analysis of lath martensite in ferrite-martensite dual phase steel sheet annealed after cold-rolling. ISIJ Int. 55 (10), 2198–2205.